

Noise-resilient solid host for electron qubits above 100 mK

Xinhao Li,^{1,2} Christopher S. Wang,³ Brennan Dizdar,³ Yizhong Huang,^{4,5} Yutian Wen,⁶ Wei Guo,^{7,8} Xufeng Zhang,⁵ Xu Han,^{1,4, a)} Xianjing Zhou,^{7,8, b)} and Dafei Jin^{1,6, c)}

¹⁾ Center for Nanoscale Materials, Argonne National Laboratory, Lemont, Illinois 60439, USA

²⁾ Department of Physics, Harvard University, Cambridge, Massachusetts 02138, USA

³⁾ James Franck Institute and Department of Physics, University of Chicago, Chicago, Illinois 60637, USA

⁴⁾ Pritzker School of Molecular Engineering, University of Chicago, Chicago, Illinois 60637, USA

⁵⁾ Department of Electrical and Computer Engineering, Northeastern University, Boston, Massachusetts 02115, USA

⁶⁾ Department of Physics and Astronomy, University of Notre Dame, Notre Dame, Indiana 46556, USA

⁷⁾ National High Magnetic Field Laboratory, Tallahassee, Florida 32310, USA

⁸⁾ Department of Mechanical Engineering, FAMU-FSU College of Engineering, Florida State University, Tallahassee, Florida 32310, USA

(Dated: 19 February 2025)

Cryogenic solid neon has recently emerged as a pristine solid host for single electron qubits. At ~ 10 mK temperatures, electron-on-solid-neon (eNe) charge qubits have exhibited exceptionally long coherence times and high operation fidelities. To advance this platform towards a scalable quantum information architecture, systematic characterization of its noise feature is imperative. Here, we show the remarkable resilience of solid neon against charge and thermal noises when eNe qubits are operated away from the charge-insensitive sweet-spot and at elevated temperatures. Without optimizing neon growth, the measured charge (voltage) noise on solid neon is already orders of magnitude lower than that in most stringently grown semiconductors, rivaling the best records to date. Up to 400 mK, the eNe charge qubits operated at ~ 5 GHz can maintain their echo coherence times over 1 microsecond. These observations highlight solid neon as an ideal host for quantum information processing at higher temperatures and larger scales.

Solid-state electron qubits are inherently affected by decoherence mechanisms in their host materials. Spectral characterization has revealed a typical $1/f$ noise distribution for both charge and spin qubits, often attributed to individual charge fluctuators at the surfaces and interfaces of semiconductor or superconducting materials¹⁻³. Extensive effort has been made to extend electron qubit coherence times by reducing the noise density in the surrounding environment and minimizing the sensitivity of qubits to noise^{2,4,5}. Recently, we demonstrated solid neon as a novel host material that traps electrons at the neon-vacuum interface^{6,7}. Using a circuit quantum electrodynamics architecture, we address the charge states of eNe by coupling them to superconducting resonators. At the charge sweet-spot, eNe qubits are first-order insensitive to charge noise, showing long coherence times T_2^* of up to ~ 50 μ s (ref⁷), which is nearly four orders of magnitude longer than that of reported semiconductor charge qubits⁸. This behavior can be favorably translated to eNe *spin* qubits as well with even better predicted performance⁹⁻¹¹.

There remains, however, more to be understood about the nature of eNe charge qubits (which we will refer to as “eNe qubits” for the remainder of the manuscript) and their environment. The specific electron trapping mechanism on solid neon is unclear, though it is likely that disorder in the neon surface plays a key role¹². Moreover, the environmental coherence-limiting factors in current devices remain elusive. Investigating the performance of eNe qubits away from the sweet-spot and at elevated temperatures, when the qubit is subject to charge and thermal noise, can provide valuable insight into the coupling between eNe and the environment, revealing the role of the neon host and paving the way for improved qubit performance and stability. This is crucial for scaling up the eNe qubit platform, as environmental noise is a major obstacle to the precise creation and consistent retention of entangled multi-qubit states^{1,13}. It is also essential for understanding the limitations of spin-state control^{2,9,14} of eNe using electrically sensitive mechanisms such as synthetic spin-orbit coupling¹⁵⁻¹⁹ or exchange interactions²⁰⁻²³. Furthermore, operating qubits at elevated temperatures can mitigate many engineering constraints due to limited cooling power at base temperature, advantageous for scaling²⁴⁻²⁶.

In this work, we utilize individual eNe qubits as probes for evaluating solid neon as a robust electron qubit host. We study the coherence and noise behavior of eNe qubits under both on- and off-sweet-spot conditions, as well as their temperature-dependent coherence up to 0.5 K. When the qubit is biased to be sensitive to charge noise, dynamical decoupling (DD) effectively extends eNe’s coherence toward the relaxation limit ($2T_1$). Notably, the extracted high-frequency charge noise density via DD measurements, projected as voltage fluctuation on the nearby electrode of eNe, can be orders of magnitude smaller than what electron qubits experience in semiconductor materials¹⁵⁻²¹, approaching some of the best performance²³. Meanwhile, the varying qubit and noise properties across different eNe qubits reflect the complexity of the local charge environment of individual electrons, likely due to the disordered neon surface and adjacent excess electrons. Furthermore, we found that the thermal resilience of eNe qubits with a frequency of

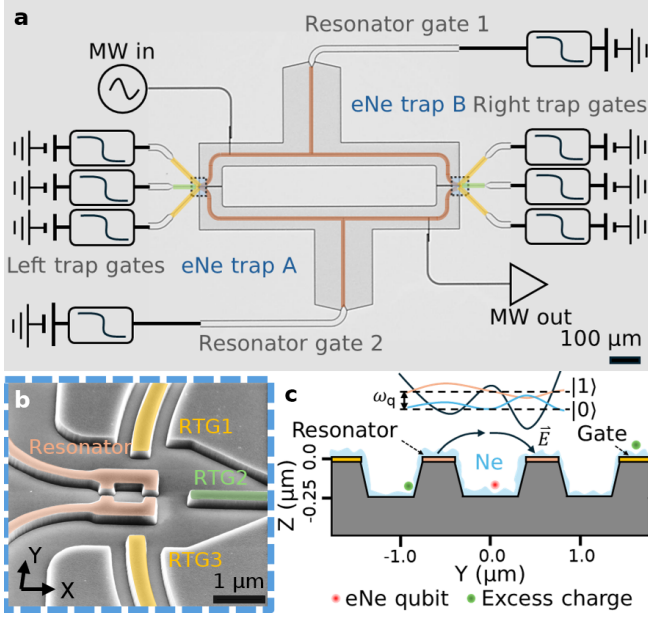


Fig. 1. eNe charge qubit coupled to a TiN high-impedance superconducting resonator. **a**, Illustration of the high impedance TiN superconducting resonator with two identical electron traps. Microwave (MW) signals to control and read out the electron qubit’s charge state are sent through the resonator via the input and output ports. Gate electrodes are patterned with on-chip low-pass filters to apply DC bias voltage to the qubits while maintaining the resonator’s quality factor. The metal plane between the resonator pins is connected to the ground plane via aluminum wire bonds. **b**, False-color scanning electron micrograph image of the electron trapping area on the right side of the resonator with trap gates (RTG). **c**, Cross-section schematic of the electron trapping area.

~ 5 GHz supports echo coherence times exceeding 1 μ s up to 400 mK, primarily limited by thermally induced increases in energy relaxation and dephasing rates. These results highlight the superior noise isolation the neon host provides and the importance of engineering the local charge environment to enhance performance uniformity.

Device structure

Our device consists of a split superconducting resonator made of a 30 nm thick TiN film grown on a (111)-oriented intrinsic silicon (Si) substrate by atomic layer deposition²⁷, as shown in Fig. 1a. An electron trap is positioned at each end of the resonator, with the broader goal of coupling two distant eNe qubits via the resonator bus²⁸. Each electron trap features a simplified rectangular structure compared to the previously used oval-shaped design^{6,7}. Around the traps, the Si substrate is etched down by approximately 250 nm to host the thin neon layer, as illustrated in Fig. 1b. In this work, we utilize the differential mode of the resonator to couple to motional states of electrons trapped on solid neon

(see Supplementary I), with the microwave electrical field pointing from one resonator pin to the other²⁹, as shown in Fig. 1c. Considering the first two charge states of eNe, the coupled system can be described by the Jaynes-Cummings Hamiltonian¹⁴:

$$H = \hbar\omega_r \left(a^\dagger a + \frac{1}{2} \right) + \frac{1}{2} \hbar\omega_q \sigma_z + g(a^\dagger \sigma_- + a \sigma_+), \quad (1)$$

where $\omega_r/2\pi = 5.668$ GHz is the resonator frequency after neon deposition, $\omega_q/2\pi$ is the qubit transition frequency, g is the electron-photon coupling strength, a^\dagger and a are the photon creation and annihilation operators, respectively, σ_z and $\sigma_\pm \equiv \sigma_x \pm i\sigma_y$ are the standard Pauli operators on a two-level system.

As an improvement from previous work, we leverage the high kinetic inductance (~ 20 pH/ \square) of the thin TiN film to enhance the qubit-resonator coupling strength³⁰. The estimated equivalent lumped element impedance for the differential mode is $Z_r \sim 600 \Omega$ (see Supplementary I), approximately ten times that of the previous niobium (Nb) device^{6,29}. Since $g \propto \omega_r \sqrt{Z_r}$, we expect the high impedance resonator to support a coupling strength achieving $g/2\pi \sim 10$ MHz level³⁰. Meanwhile, several DC gates are placed around the electron trapping area to tune the qubit transition frequency, as shown in Fig. 1a-b. In order to minimize microwave leakage of the resonator mode through the DC gates, all gates are equipped with on-chip low-pass filters with a ~ 0.5 GHz cutoff frequency providing over 60 dB attenuation at resonator frequency. This is particularly important in our device given that for high-impedance resonators, the parasitic gate capacitance can be comparable to the resonator capacitance^{31,32}. With this design, the resonator maintains a narrow linewidth $\kappa/2\pi$ of 0.38 MHz (see Supplementary I). Before performing electron experiments, a thin layer of neon was grown on the surface of the device following the same procedure as in our previous work⁷, resulting in less than 1 MHz redshift of the resonator frequency. Electrons are emitted from a tungsten filament and bound to the surface of the neon film. Only when both the neon film is present on the sample surface, and electrons are emitted do we see signatures of trapped eNe qubits strongly coupled to the resonator (see Supplementary II).

Qubit performance

As illustrated in Fig. 1c, the local neon profile and the trap structure define the potential energy landscape seen by the electrons. Recent theoretical work emphasized the neon surface’s important role in defining the qubit’s Hamiltonian¹², whose exact form remains unclear. Here, we approximate each eNe qubit’s transition frequency with a generalized hyperbolic model, capturing the measured qubit spectroscopic features:

$$\hbar\omega_q = \sqrt{\hbar^2(\omega_{ss} + \delta\omega_{ss})^2 + (\epsilon + \delta\epsilon + 2d_e(\mathcal{E} + \delta\mathcal{E}))^2}, \quad (2)$$

where ω_{ss} represents the the charge sweet-spot frequency, and ϵ describes the energy off-set defining the

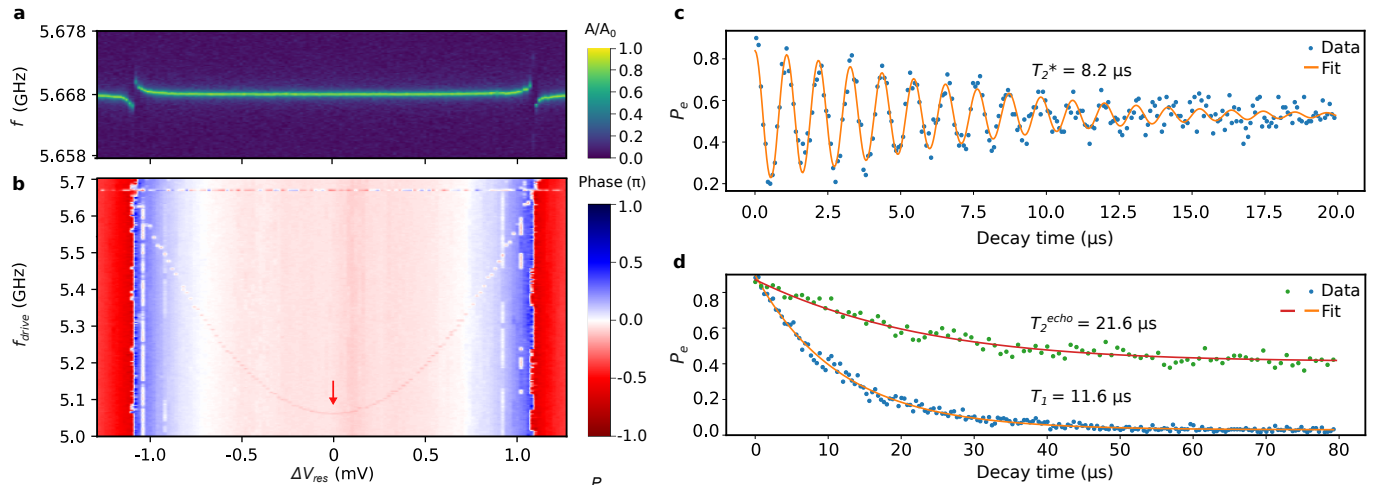


Fig. 2. Spectroscopic and coherence properties of an eNe charge qubit Q1. **a**, Normalized microwave transmission amplitude (A/A_0) centered around the resonator frequency versus the relative resonator bias voltage ΔV_{res} as described in **b**. Two avoided crossings appear when the eNe qubit comes into resonance with the resonator. **b**, Two-tone qubit spectroscopy measurement displaying the transmission phase response at the resonator frequency ω_r versus ΔV_{res} , for weak probe tones concurrently sent in at f_{drive} . **c**, Ramsey fringes at the charge sweet-spot, marked with the red arrow in **b**, with fitted T_2^* of $8.2 \mu\text{s}$. P_e is the qubit's excited-state population. **d**, Relaxation and Hahn echo measurements showing $T_1 = 11.6 \mu\text{s}$ and $T_2^{\text{echo}} = 21.6 \mu\text{s}$ at the charge sweet-spot.

corresponding bias voltage. This model has been widely applied to describe two-level quantum systems³³, with an energy landscape consistent with our bounds of large anharmonicity in eNe charge qubits⁷. The electrical tunability of the qubit's transition frequency is described by the term $2d_e\mathcal{E}$, where d_e is the electron dipole moment and \mathcal{E} is the applied field^{34–36}. Meanwhile, noise terms $\delta\mathcal{E}$, $\delta\epsilon$ and $\delta\omega_{\text{ss}}$ caused by DC bias or adjacent charge fluctuations lead to qubit decoherence.

Bringing eNe qubit's transition frequency ω_q onto resonance with ω_r results in the vacuum Rabi splitting in the resonator's transmission spectrum. An example of this is shown in Fig. 2a for Q1, one of the three qubits we characterized, with the electron-photon coupling strength $g/2\pi = 6.43 \text{ MHz}$ and on-resonance qubit linewidth $\gamma/2\pi = 3.81 \text{ MHz}$ (see Supplementary III-VI for details of characterizations on the three qubits Q1-3). Compared to the previous Nb resonator^{6,7}, the higher impedance of the TiN resonator enhances the qubit-resonator coupling strength, with a maximum observed $g/2\pi$ of approximately 16 MHz (see Q3 in Supplementary VI). We further mapped the qubit spectrum by applying a second drive tone and probing at the resonator frequency at low power, as shown in Fig. 2b. The extracted qubit frequency follows a hyperbolic dependence on the DC voltage V_{res} applied to the resonator with a charge sweet-spot at 5.065 GHz (see Supplementary IV). The sweet-spot frequency, coupling strength, and sensitivity to DC biases ($\partial f_q/\partial V_{\text{res}}$) vary between qubits (see Supplementary III). This variation suggests some randomness in the local trapping potential, which determines the qubit's

minimum transition frequency and the projection of the electron's dipole moment along the resonator mode and the applied DC field.

Next, we characterize the coherence performance of the qubit biased at its charge sweet-spot. Figure 2c-d show the measured T_1 , T_2^* , and T_2^{echo} of $11.6 \mu\text{s}$, $8.2 \mu\text{s}$, and $22.6 \mu\text{s}$, respectively. Unlike the qubit reported in our previous works⁷, the relaxation time (T_1) of eNe qubits observed on the new TiN device is generally not Purcell-limited at their charge sweet-spots, with over 100 MHz detuning from the resonator ($\Delta_{\text{rq}}/2\pi$). The Purcell rate of Q1 to the resonator mode is $\Gamma_r = \kappa g^2/\Delta_{\text{rq}}^2 = 1/3.9 \text{ ms}^{-1}$, which indicates that non-radiative decay channels dominate the energy relaxation of Q1. Measurements of the Q1's T_1 at various bias frequencies (see Noise Spectroscopy section) further confirm that the non-radiative decay dominates the energy relaxation unless the qubit frequency is tuned much closer to the resonator frequency. Additionally, the fact that the T_2^{echo} approaches $2T_1$ indicates that the quasi-static noise is the dominating dephasing factor for Q1 at its charge sweet-spot^{37,38}.

Noise spectroscopy

Fluctuations in the charge environment can cause stochastic frequency shifts of the eNe qubit, which leads to qubit dephasing. Armed with high fidelity control and a known voltage (charge) lever arm, we first characterize the high-frequency noise spectral density of Q1 using the Carr-Purcell-Meiboom-Gill (CPMG) sequence with $N = 0, 1, 2, 4, 6, 8, 12, \text{ and } 16$ refocusing pulses. All bias points had positive ΔV_{res} as shown in Fig. 2b, with a maximum

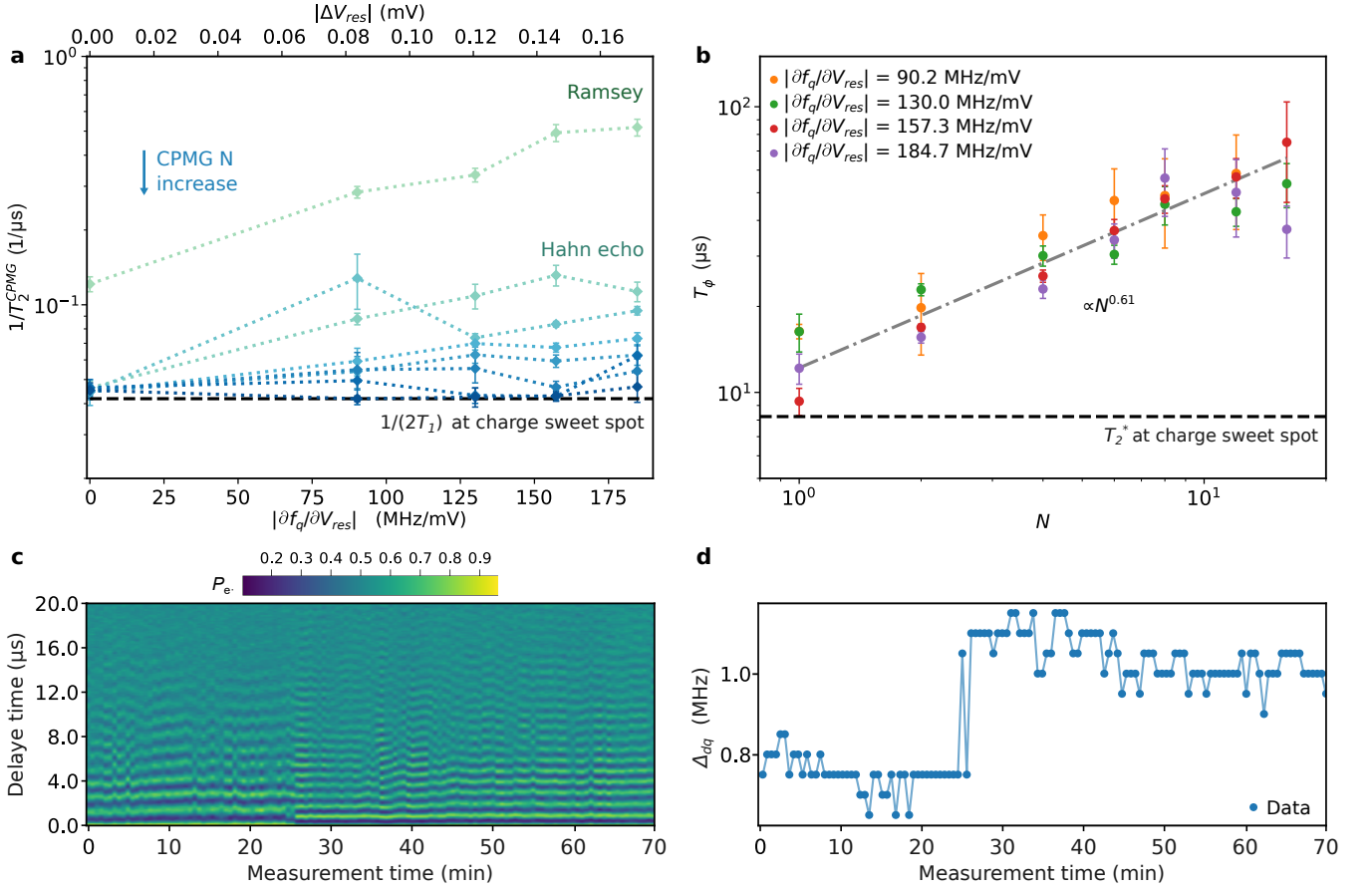


Fig. 3. Decoherence of eNe qubit Q1. **a**, Calculated $1/T_2^{\text{CPMG}}$ for various qubit bias points and refocusing pulse numbers N . With the increase of N , the $1/T_2^{\text{CPMG}}$ of the qubit biased near the charge sweet-spot approaches the limit of $2T_1$. **b**, The pure dephasing time T_ϕ increases as a function of N when the qubit biased away from charge sweet-spot, with a power-law fit of $T_\phi \propto N^{0.61}$. **c**, Repeated Ramsey fringes measured near qubit sweet-spot for 128 iterations, with each record taking 33 s. **d**, Detuning Δ_{dq} between drive tone and qubit frequency during the Ramsey measurements, revealing stochastic frequency shifts.

sensitivity of $\partial f_q/\partial V_{\text{res}} = 180.7$ MHz/mV, corresponding to a qubit frequency detune of 15.9 MHz from the charge sweet-spot. The measured average energy relaxation time at all bias points is $11.94 \pm 0.3 \mu\text{s}$, indicating that the same non-radiative decay channel dominates. We fit the measured coherence decay to extract the decoherence time T_2^{CPMG} and pure dephasing time T_ϕ (See Methods). As shown in Fig. 3a, in the absence of refocusing pulses (i.e., the Ramsey measurement), the decoherence rate $1/T_2^{\text{CPMG}}$ increases with sensitivity to charge noise. At $\partial f_q/\partial V_{\text{res}} = 180.7$ MHz/mV, T_2^* decreases to $1.93 \mu\text{s}$. Introducing refocusing pulses enhances T_2^{CPMG} at every biasing point, approaching two times of T_1 as N increased. At the charge sweet-spot, the rapid saturation of T_2^{CPMG} with increasing N indicates a low noise power density in the relatively high-frequency range (100 kHz). When the qubit was biased at a point more sensitive to charge noise, more pulses were required to extend the T_2^{CPMG} towards the energy relaxation limit. In Supplementary V and VI, we show that for the other two eNe qubits, a single refocusing pulse is insufficient to

mitigate the majority of noises at the qubits' sweet-spot, suggesting a higher noise density at the high-frequency range. This variation in noise behavior suggests some complexities of the local noise environment experienced by individual electrons on the neon surface.

Figure 3b plots the fitted pure dephasing time (T_ϕ) at bias points away from the sweet-spot as a function of the number of refocusing pulses (N). The relation between T_ϕ and N reflects the frequency-dependent noise power distribution. For a noise spectrum following $S(f) \propto 1/f^\alpha$, T_ϕ should scale with N^β , where $\beta = \alpha/(1 + \alpha)$ (ref. 17,20,21,39). The fitted β via this scaling relation provides a more accurate noise distribution compared to individual fittings of the decay curve using $\chi_N(\tau) = (\tau/T_\phi)^{\alpha+1}$ (ref. 39). For Q1, the average fitting gives $\beta = 0.61$, corresponding to $\alpha = 1.56$.

In the 100 kHz frequency range of Fig. 4, we plot the calculated total noise in the unit of Hz^2/Hz , for the four different bias points away from the charge sweet-spot. (See Methods for details of the CPMG sequence and noise calculation.) The extracted total noise scales

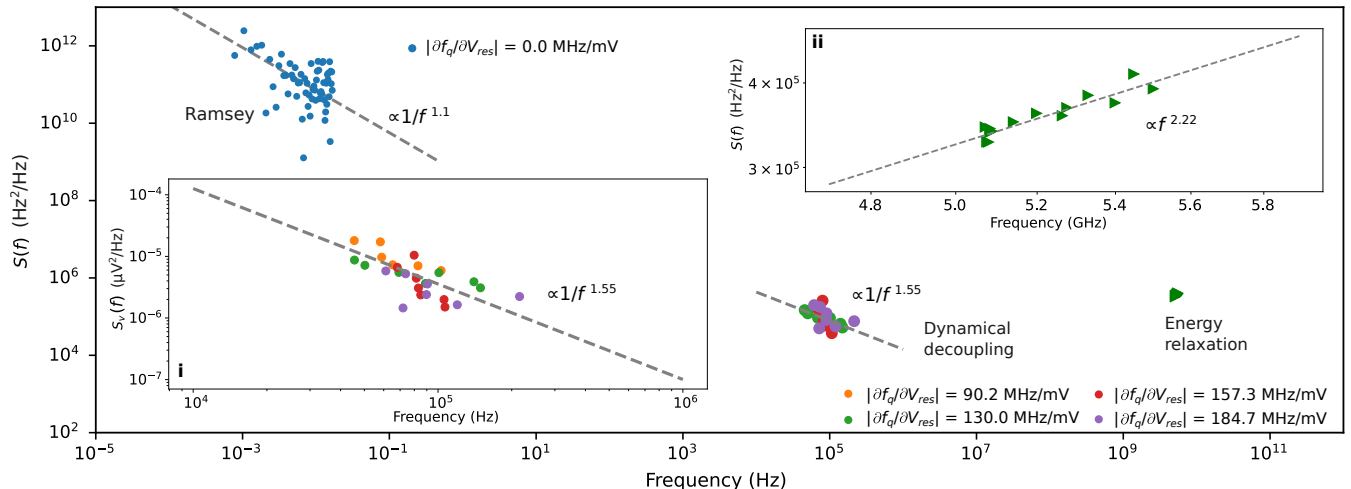


Fig. 4. Noise spectroscopy of eNe qubit Q1. Main plot between 0.01 \sim 1 MHz: Total noise density (colored dots) derived from dynamical decoupling data at different qubit bias points. Main plot between 10^{-3} to 10^{-1} Hz: Calculated total noise density (blue dots) from long-term Ramsey measurements when biased at charge sweet-spot. Main plot near 5 GHz: Transverse noise of the eNe qubit (green triangles). Inset plot i: Equivalent charge (voltage) noise on the resonator electrode. Inset plot ii: Zoom-in of transverse noise. Gray dashed lines: Power-law fits of frequency-dependent noise.

from 10^6 to 10^4 Hz^2/Hz as the frequency increases, with an averaged power-law fitting of $S \propto 1/f^{1.55}$, matching the fitting result in Fig. 3b. The spectral noise behavior observed away from the sweet-spot suggests that charge noise dominates the total noise when the qubit is more sensitive to electrical fluctuation. Given the qubit’s sensitivity to V_{res} and neglecting other potential noise sources, we can extract the equivalent voltage (charge) noise as fluctuations of the DC voltages applied on the resonator electrodes. The inset in Fig. 4 shows the calculated charge noise of $S_v \sim 10^{-5}$ $\mu\text{V}^2/\text{Hz}$ at the 100 kHz frequency range. A separate measurement on Q2 gives a similar charge noise density with $S_v \propto 1/f^{1.14}$ (see Supplementary V and Discussion and Outlook).

To benchmark different electron qubit material platforms, we compare the environmental charge noise measured as voltage fluctuations on adjacent gate electrodes, situated at a distance on the scale of one hundred nanometers from the qubits. Specifically, we examine electrons trapped on solid neon and those confined in semiconductor materials, which are the leading platforms for hosting electron qubits. Table 1 summarizes our results on eNe and compares them with data from the literature on semiconductor qubits. Because of the clean qubit environment provided by the neon interface, the charge noise experienced by eNe is orders of magnitude lower than that in typical semiconductor materials, approaching some of the best performance. Given the smaller susceptibility of electron spin qubits to charge noise through effects including spin-orbit coupling and exchange interactions, as shown in the “ $\partial f_q/\partial V$ ” column of Tab. I, we foresee that electron spin qubits on solid neon could approach a pure dephasing

time of millisecond-scale⁹. The development of the electron trap and the suppression of redundant electrons on neon will further improve the qubit performance.

After investigating the high-frequency noise, we turn to the low-frequency noise at the charge sweet-spot. Figure 3c-d show variations in Q1’s frequency revealed by performing repeated Ramsey measurements^{20,21} for approximately one hour since initially biased near its charge sweet-spot. The qubit undergoes a discrete frequency transition of varying magnitudes, as seen near the 25 minutes of the one-hour tracing. This is revealed by a Fast Fourier transform (FFT) of the Ramsey signals (See Methods and Supplementary IV). It suggests slow mechanisms driving qubit decoherence, akin to low-frequency dynamics in semiconductor and superconducting qubits^{20,21,40}, which can be mitigated with feedback control^{41,42}. Using a periodogram method, we convert this one-hour qubit frequency measurement into a frequency noise spectrum over 10^{-3} to 10^{-1} Hz, as shown in Fig. 4. A power-law fit of the data gives the relation of $S \propto f^{-1.11}$. Despite the qubit being first-order insensitive to small charge (voltage) fluctuation at the sweet-spot, it can still experience slow frequency drifts due to nearby charge fluctuations, as observed in both semiconductor and superconducting qubits via second-order effects^{43,44}. Other detection methods, such as single-electron charge sensing techniques²¹, could complete the noise spectrum ranging from 1 Hz to 10^4 Hz.

To complete the discussion, we calculate the transverse noise at the qubit frequencies contributing to energy relaxation with $1/T_1 = \pi/2 \times S(2\pi f_q)$ (ref.³⁷). The fitted total transverse noise versus frequency follows

Material platform	Qubit type	S_v ($\mu\text{V}^2/\text{Hz}$)	Noise frequency (kHz)	$\partial f_q/\partial V$ (MHz/mV)	Reference
Neon	single-electron charge	$10^{-5} \sim 10^{-7}$	10 ~ 1000	10 ~ 100	this work
Si/SiO ₂	singlet-triplet spin	$10^{-1} \sim 10^{-2}$	100 ~ 1000	~ 10	ref. ²⁰
Si/SiO ₂	single-electron spin	$10^{-1} \sim 10^{-2}$	10 ~ 100	0.2	ref. ¹⁵
²⁸ Si/ ²⁸ SiO ₂	single-electron spin	$10^0 \sim 10^{-1}$	1 ~ 10	0.01	ref. ¹⁶
Si/SiGe	singlet-triplet spin	$10^{-4} \sim 10^{-5}$	100 ~ 1000	~ 10	ref. ²¹
Si/SiGe	single-electron spin	$10^{-1} \sim 10^{-3}$	10 ~ 1000	0.55	ref. ¹⁹
²⁸ Si/SiGe	single-electron spin	$10^{-2} \sim 10^{-3}$	10 ~ 100	0.09	ref. ¹⁷
²⁸ Si/SiGe	single-electron spin	10^{-1}	10	0.36	ref. ¹⁸
²⁸ Si/SiGe	singlet-triplet spin	$10^{-2} \sim 10^{-4}$	10 ~ 1000	4.5	ref. ²²
GaAs/AlGaAs	singlet-triplet spin	$10^{-7} \sim 10^{-8}$	100 ~ 1000	10 ~ 100	ref. ²³

Tab. I. Comparison between voltage noises experienced by electron qubits on solid neon and in semiconductor material platforms.

$S \propto f^{2.22}$ between 5.065 to 5.498 GHz, with a mean of $3.6 \times 10^5 \text{ Hz}^2/\text{Hz}$, as shown in the inset of Fig. 4.

Temperature dependence

To obtain more information about the noise environment of eNe qubits, we measured the temperature dependence of Q1's coherence (T_1 , T_2^* , and T_2^{echo}) at its charge sweet-spot from 10 mK to 500 mK. The energy relaxation T_1 is well described by a model that only accounts for the coupling of a two-level quantum system to a bosonic thermal bath within the experiment's temperature range, $T_1 \propto \tanh(\hbar\omega_q/2k_B T)$ (Fig. 5a) (ref. ^{45,46}). Similarly, the thermal population follows that of a Maxwell-Boltzmann distribution ⁴⁷ (See Supplementary IV). The corresponding single electron temperature closely tracks the mixing-chamber (MXC) temperature between 100 to 500 mK and saturates around 40 mK, as shown in Fig. 5a. This effective cooling of electron qubits below 100 mK is difficult to achieve with electrons in semiconductors, due to the suppressed electron-environment interaction at low temperatures ⁴⁸.

A separate measurement on a different qubit Q2, presented in Supplementary V, also reveals strikingly thermal behavior in T_1 and thermal population but with a different T_1 in the low-temperature limit. It suggests a picture in which individual eNe qubits couple differently to their environment (perhaps through phonons ^{9,14}), which sets the low temperature T_1 . This motivates further studies of the microscopic limitations of T_1 . At these qubit frequencies, T_1 drops to only about half the low-temperature value at 200 mK, facilitating operation at higher temperatures. In contrast, electron qubits in semiconductor materials are susceptible to phonon effects ^{25,49}, which can significantly degrade T_1 at elevated temperatures. Given these favorable scalings, we can also anticipate further improvement of the high-temperature performance of eNe qubits by engineering the electron trapping and detection structure to support charge- or spin-qubit operations at higher frequencies ²⁴.

The temperature dependence of the coherence data, however, remains complex. T_2^* and T_2^{echo} show that quasi-static and high-frequency noise components behave differently with temperature, as shown in Fig. 5b. With

increasing temperature, $T_2^* \propto T^{-0.74}$, indicating the quasi-static noise power scales almost linearly against temperature. Below 50 mK, T_2^{echo} approaches $2T_1$, suggesting that the single echo pulse still effectively mitigates the quasi-static noise that contributes to most of the dephasing. However, starting from 75 mK, T_2^{echo} scales with temperature as $\propto T^{-1.1}$, and quickly degrades from $2T_1$, indicating the rise of non-quasistatic dephasing noises at higher temperatures ²³. Despite that, Q1 maintains $>1 \mu\text{s}$ T_2^{echo} at elevated temperatures up to 400 mK with qubit frequency only at ~ 5 GHz, showing eNe's thermal-resilient coherence performance and potential for high-temperature operation.

We then extract the relation between the pure dephasing time (T_ϕ) and MXC temperature, following the coherence decay formula described in the Methods. As shown in Fig. 5c, T_ϕ begins to decrease significantly when the MXC temperature exceeds 100 mK. In this range, the measured data matches well with a parameter-free model accounting for the effect of resonator thermal photon on the qubit dephasing ^{24,50}:

$$T_\phi^{-1} = \frac{\kappa}{2} \text{Re} \left[\sqrt{\left(1 + \frac{2i\chi}{\kappa}\right)^2 + \frac{8i\chi}{\kappa} n_{\text{th}} - 1} \right] \quad (3)$$

where κ is the resonator decay rate, and χ is the resonator's dispersive shift (see Supplementary IV). n_{th} represents the resonator thermal photon population, equal to $1/(e^{\hbar f_r/k_B T} - 1)$. At higher temperatures, qubit coherence is degraded primarily due to thermal effects. Nevertheless, the data's deviation from the model below 100 mK suggests the presence of other low-temperature dephasing mechanisms. Separate measurements on Q2 (Supplementary V) give similar results.

Discussion and outlook

In this work, we have quantitatively evaluated, for the first time, the environmental noise isolation provided by the thin neon layer for eNe qubits, demonstrating a number of distinct advantages compared to semiconductor host materials for single electron qubits. Additionally, eNe qubits exhibit thermally resilient coherence, making them promising for high-

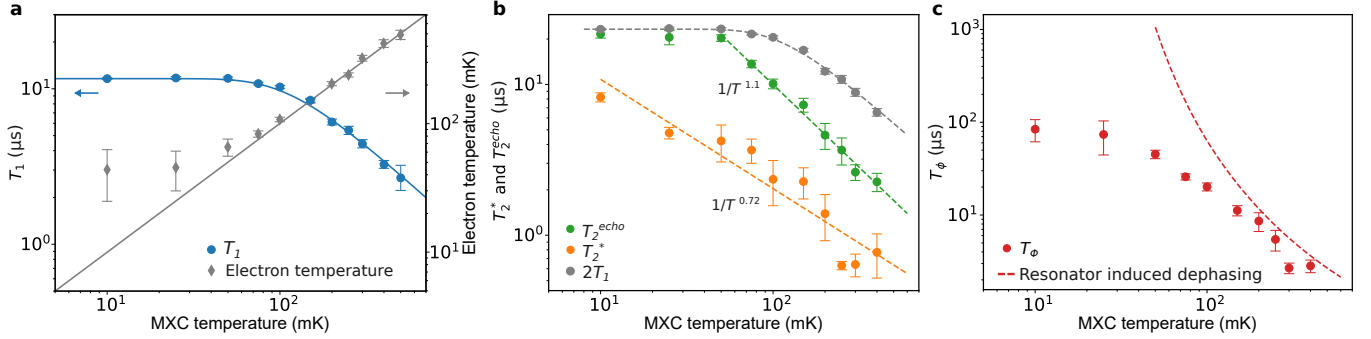


Fig. 5. Temperature-dependent coherence of eNe qubit Q1 at charge sweet-spot. **a**, T_1 (blue dots, data) versus mixing chamber (MXC) temperature. The solid curve represents the predicted decay rate $T_1(T) = T_1(T=0) \cdot \tanh(\hbar\omega_q/2k_B T)$ where we use the measured value at 10 mK for $T_1(T=0)$. Extracted electron temperature (gray diamonds, data) versus MXC temperature based on the measured thermal population in Supplementary IV. **b**, Decoherence time, T_2^* (orange dots) and T_2^{*echo} (green dots) versus the MXC temperature, with power-law fitting. Gray dots and curves show $2T_1$ for comparison. **c**, Extracted pure dephasing time T_ϕ as a function of the MXC temperature. Red dashed curve: Parameter-free calculation of the resonator-induced dephasing based on Q1 properties.

temperature operation. These systematic coherence and noise characterization highlight the following directions for future research.

The inconsistent spectral properties of eNe qubits indicate that the local neon profile is crucial in electron-trapping mechanisms. Variations in the neon surface profile, caused by liquid-phase solidification and substrate roughness, introduce randomness in the energy potential landscape that hosts the electron qubits. Additionally, the relative position of trapped electrons to nearby electrodes determines the frequency lever-arm and the qubit's sensitivity to voltage fluctuations. To enhance consistency and control over individual qubit properties, refined neon growth methods, and gate-defined electron trapping mechanisms should be developed to mitigate the effects of neon surface randomness.

On the other hand, diverse noise behavior observed in eNe qubits reflects the complexity of the local charge environment. The inconsistent spectral noise distribution suggests locally non-uniform noise sources. Theoretical studies have shown the high sensitivity of qubit's coherence to fluctuators' density and distribution⁵¹. Excess electrons emitted by the tungsten filament could result in artificial charge fluctuators with high mobility on the neon surface. This charge rearrangement can further contribute to the low-frequency qubit drift and occasional electron escape events⁵². Strategies include developing electron loading procedures²⁹ and protection gates to separate trapped qubits from adjacent charge reservoirs²⁵ could be implemented to improve the qubit's stability.

Finally, the limiting factor for the non-radiative energy relaxation rate of eNe qubits needs further investigation. The non-monotonic variations in T_1 of qubits with different charge sweet-spot frequencies point to localized non-radiative decay channels. Nearby

charges may create a sparse bath of two-level fluctuators weakly coupled to the eNe qubit, whose density determines the transverse noise intensity^{51,53}. Electrical manipulations could be applied to bias or repeal those weakly coupled charges to reduce the relaxation rate⁵⁴. With the development of improved electron loading and trapping methods, we foresee the improvements in both the coherence and long-term stability of eNe qubits.

Methods

Device and setup

The resonator, electrode, and on-chip filter were patterned with electron beam lithography followed by reactive-ion etching. See details of the TiN film, resonator, and on-chip filter characterization in Supplementary I. The experiment setup is similar to the ones in our previous works^{6,7}. The chip was mounted on a customized printed circuit board within a vacuum-sealed copper cell, which provides direct current (DC) and microwave (MW) interfaces. On the top lid of the cell, a gas filling line was attached to deposit neon at cryogenic temperature, and a tungsten filament was used as the electron source. The cell is mounted on the mixing chamber (MXC) plate of a dilution refrigerator. A total attenuation of 60 dB was applied on the cryogenic segment of the MW input line with infrared filters (QMC-CRYOIRF-004). The MW output line was equipped with cryogenic isolators (LNF-ISISC4_12A) at the MXC plate, followed by a high electron mobility transistor (LNF-LNC4_8C) at 4K plate and room temperature amplification. All DC connections were filtered with thermocoaxes cable, LC filters (Mini-Circuits RLP-30+), and homemade low-pass filters with 150 Hz cutoff. Qubit spectroscopic measurements were conducted with a vector network analyzer (Keysight N5222B) and a signal generator (Anritsu MG3692C). Time-domain pulse measurements were conducted with

Quantum Machine OPX+ and Octave. The DC gates were applied with QDevil QDAC-II.

Neon growth

Neon is filled with the following procedure. The fridge is warmed up from its base temperature with a heater mounted on the 4 K plate. At this moment, the helium mixture circulation is turned off, and all the mixture has been collected while the pulse tube is still on. The heater power is set to a value such that it creates a temperature gradient from 27 K at the 4 K plate to about 25 K at the MXC plate. Under such conditions, the neon gas is filled and deposited onto the device chip in its liquid phase. After filling, the heater is turned off, and the whole fridge is cooled down again to let the liquid neon freeze into solid. During the cool down, we further anneal the neon film at 10 K for 1 hour.

Electron deposition

Electrons are ejected from the tungsten filament mounted on the lid of a hermetic copper cell. When the dilution fridge is cooled down to the base temperature, the total resistance on the filament loop is 2Ω . A current pulse train applied by a pulse generator with -0.6 V voltage output, pulse width of 0.1 ms, repetition frequency of 1 kHz, and duration of 0.3 s was used to fire electrons. We noticed that applying higher voltage or longer duration would cause too many electrons to land on the top of the chip, reducing the stability of the trapped electrons.

Noise characterization

We use the dynamical decoupling technique with Carr-Purcell-Meiboom-Gill (CPMG) pulse sequences to study the spectral distribution of high-frequency noise affecting the eNe qubits^{37,38}. In the sequence, N refocusing Y_π pulses are applied between two $X_{\pi/2}$ pulses with identical separation τ/N between two pulses. Under such sequences, qubits' coherence decaying follows $P_e(N, \tau) = P_0 + a \cdot \exp(-\tau/2T_1) \exp(-\chi_P) \exp(-\chi_N(\tau))$, accounting for pure dephasing $-\chi_N$, energy relaxation $-\tau/2T_1$, and decay during driving pulses $-\chi_P$ (ref.³⁷). We define T_2^{CPMG} as the time when the qubit's coherence decays by a factor of $1/e$ due to energy relaxation and pure dephasing. Increasing the number of Y_π pulses reduces the time the qubit is exposed to noise before each refocusing, thereby extending the coherence time. Under Gaussian noise assumption^{37,38}, a CPMG sequence with N refocusing pulses and total delay time of τ imposes a filter function $g_N(\omega, \tau)$ to the qubit noise caused by source λ with spectral distribution $S_\lambda(\omega)$, which determines the qubit's dephasing $\chi_N(\tau)$:

$$\chi_N(\tau) = \tau^2 \sum_{\lambda} \left(\frac{\partial \omega_q}{\partial \lambda} \right)^2 \int_0^\infty S_\lambda(\omega) g_N(\omega, \tau) d\omega \quad (4)$$

where $\partial \omega_q / \partial \lambda$ is the qubit transition frequency's sensitivity to noise source λ , the filter function $g_N(\omega, \tau) =$

$$|y_N(\omega, \tau)|^2 / (\omega\tau)^2, \text{ and } y_N(\omega, \tau) = 1 + (-1)^{1+N} \exp(i\omega\tau) + 2 \sum_{j=1}^N (-1)^j \exp(i\omega\tau(j-0.5)/N) \cos(\omega\tau\pi/2).$$

With the noise filter imposed by the CPMG sequence, we could approximate the total noise power spectrum density S at frequency f_N as (ref.^{20,21}):

$$S(2\pi f_N) = \frac{1}{(T_\phi)^2 g_N(2\pi f_N, T_\phi) \Delta\omega_N} \quad (5)$$

where $2\pi f_N$ is the peak angular frequency of the first harmonic of $g_N(\omega, T_\phi)$, and $\Delta\omega_N$ is the full width at half maximum of the peak.

To investigate the low-frequency dynamics of qubit decoherence near the charge sweet-spot, we repeatedly conducted Ramsey measurements for 128 iterations, with each recording taking 33 seconds^{20,21}. As shown in Fig. 3d, we extracted the qubit frequency drift through a fast Fourier transform (FFT) analysis of the measured Ramsey fringes. During the measurement, we also observed more drastic qubit frequency fluctuations on the scale of 10–100 MHz, corresponding to 0.14–0.44 mV in ΔV_{res} . Sometimes, we even observed the disappearance of qubit signatures in the usual gate scanning range. These qubit frequency "jumps" usually occur less than 0.5 times per hour. We attribute these large fluctuations to charge rearrangements of nearby weakly trapped electrons on neon⁵². We ensured that the qubit remained relatively stable and free from such significant fluctuations during data collection for all the presented measurements at various bias points.

Data availability

The data that support the findings of this study are available from the corresponding authors upon request. Source data are provided with this paper.

Code availability

The codes used to perform the experiments and to analyse the data in this work are available from the corresponding authors upon request.

ACKNOWLEDGMENTS

Work performed at the Center for Nanoscale Materials, a U.S. Department of Energy Office of Science User Facility, was supported by the U.S. DOE, Office of Basic Energy Sciences, under Contract No. DE-AC02-06CH11357. D. J., X. H., and X. L. acknowledge support from Argonne National Laboratory Directed Research and Development (LDRD) program. D. J. and Y. W. acknowledge support from the Air Force Office of Scientific Research (AFOSR) under Award No. FA9550-23-1-0636. D. J. and W. G. acknowledge support from the National Science Foundation (NSF) under Award No. OSI-2426768. D. J., X. Zhou, and Y. H. acknowledge support from the Julian Schwinger Foundation for Physics Research. D. J. acknowledges support from the Department of Energy (DOE) under

Award No. DE-SC0025542. B. D. acknowledges support from the NSF under Award No. DMR-1906003. C. S. W. and X. L. acknowledge support from Q-NEXT, one of the US DOE Office of Science National Quantum Information Science Research Centers. W. G. acknowledges support from the Gordon and Betty Moore Foundation through Grant DOI 10.37807/gbmf11567 and the National High Magnetic Field Laboratory at Florida State University, which is supported by the NSF Cooperative Agreement No. DMR-2128556 and the state of Florida. X. Zhang and Y. H. acknowledge support from the Office of Naval Research (ONR) Young Investigator Program (YIP) program under Award No. N00014-23-1-2144. X. H. acknowledges support from France and Chicago Collaborating in the Sciences (FACCTS) program. This work was partially supported by the University of Chicago Materials Research Science and Engineering Center, which is funded by the NSF under award number DMR-2011854. This work made use of the Pritzker Nanofabrication Facility of the Institute for Molecular Engineering at the University of Chicago, which receives support from SHyNE, a node of the NSF National Nanotechnology Coordinated Infrastructure (NSF NNCI-1542205). The authors thank David I. Schuster and Amir Yacoby for their helpful discussions.

Author contributions X. L., X. Zhou, and D. J. devised the experiment. X. L. and C. S. W. conducted the experiment. X. L. designed and fabricated the device. X. L., C. S. W., and B. D. analyzed the data. Y. H., X. Zhang, and X. H. supported the experimental measurement. Y. W. and W. G. supported the theoretical understanding. D. J. conceived the idea and led the project. X. L., C. S. W., X. Zhou, and D. J. wrote the original manuscript. All authors contributed to the work.

^aEmail: xu.han@anl.gov

^bEmail: xianjing.zhou@cea.fr

^cEmail: dfjin@nd.edu

¹E. Paladino, Y. Galperin, G. Falci, and B. Altshuler, “ $1/f$ noise: Implications for solid-state quantum information,” *Reviews of Modern Physics* **86**, 361–418 (2014).

²G. Burkard, T. D. Ladd, A. Pan, J. M. Nichol, and J. R. Petta, “Semiconductor spin qubits,” *Reviews of Modern Physics* **95**, 025003 (2023).

³G. Falci, P. J. Hakonen, and E. Paladino, “ $1/f$ noise in quantum nanoscience,” in *Encyclopedia of Condensed Matter Physics (Second Edition)*, edited by T. Chakraborty (Academic Press, Oxford, 2024) second edition ed., pp. 1003–1017.

⁴N. P. De Leon, K. M. Itoh, D. Kim, K. K. Mehta, T. E. Northup, H. Paik, B. Palmer, N. Samarth, S. Sangtawesin, and D. W. Steuerman, “Materials challenges and opportunities for quantum computing hardware,” *Science* **372**, eabb2823 (2021).

⁵A. Chatterjee, P. Stevenson, S. De Franceschi, A. Morello, N. P. de Leon, and F. Kuemmeth, “Semiconductor qubits in practice,” *Nature Reviews Physics* **3**, 157–177 (2021).

⁶X. Zhou, G. Koolstra, X. Zhang, G. Yang, X. Han, B. Dizdar, X. Li, R. Divan, W. Guo, K. W. Murch, *et al.*, “Single electrons on solid neon as a solid-state qubit platform,” *Nature* **605**, 46–50 (2022).

⁷X. Zhou, X. Li, Q. Chen, G. Koolstra, G. Yang, B. Dizdar, Y. Huang, C. S. Wang, X. Han, X. Zhang, *et al.*, “Electron charge

qubit with 0.1 millisecond coherence time,” *Nature Physics* **20**, 116–122 (2024).

⁸K. Petersson, J. Petta, H. Lu, and A. Gossard, “Quantum coherence in a one-electron semiconductor charge qubit,” *Physical Review Letters* **105**, 246804 (2010).

⁹Q. Chen, I. Martin, L. Jiang, and D. Jin, “Electron spin coherence on a solid neon surface,” *Quantum Science and Technology* **7**, 045016 (2022).

¹⁰W. Guo, D. Konstantinov, and D. Jin, “Quantum electronics on quantum liquids and solids,” *Progress in Quantum Electronics*, 100552 (2024).

¹¹A. Jennings, X. Zhou, I. Grytsenko, and E. Kawakami, “Quantum computing using floating electrons on cryogenic substrates: Potential and challenges,” *Applied Physics Letters* **124** (2024).

¹²T. Kanai, D. Jin, and W. Guo, “Single-electron qubits based on quantum ring states on solid neon surface,” *Physical Review Letters* **132**, 250603 (2024).

¹³E. Knill, “Quantum computing with realistically noisy devices,” *Nature* **434**, 39–44 (2005).

¹⁴D. Schuster, A. Fragner, M. Dykman, S. Lyon, and R. Schoelkopf, “Proposal for manipulating and detecting spin and orbital states of trapped electrons on helium using cavity quantum electrodynamics,” *Physical review letters* **105**, 040503 (2010).

¹⁵B. Klemt, V. Elhomsy, M. Nurizzo, P. Hamonic, B. Martinez, B. Cardoso Paz, C. Spence, M. C. Dartailh, B. Jadot, E. Chanrion, *et al.*, “Electrical manipulation of a single electron spin in cmos using a micromagnet and spin-valley coupling,” *npj Quantum Information* **9**, 107 (2023).

¹⁶A. Zwerver, T. Krähenmann, T. Watson, L. Lampert, H. C. George, R. Pillarisetty, S. Bojarski, P. Amin, S. Amitonov, J. Boter, *et al.*, “Qubits made by advanced semiconductor manufacturing,” *Nature Electronics* **5**, 184–190 (2022).

¹⁷J. Yoneda, K. Takeda, T. Otsuka, T. Nakajima, M. R. Delbecq, G. Allison, T. Honda, T. Kodera, S. Oda, Y. Hoshi, *et al.*, “A quantum-dot spin qubit with coherence limited by charge noise and fidelity higher than 99.9%,” *Nature nanotechnology* **13**, 102–106 (2018).

¹⁸T. Struck, A. Hollmann, F. Schauer, O. Fedorets, A. Schmidbauer, K. Sawano, H. Riemann, N. V. Abrosimov, L. Cywiński, D. Bougeard, *et al.*, “Low-frequency spin qubit energy splitting noise in highly purified 28Si/SiGe,” *npj Quantum Information* **6**, 40 (2020).

¹⁹E. Kawakami, T. Jullien, P. Scarlino, D. R. Ward, D. E. Savage, M. G. Lagally, V. V. Dobrovitski, M. Friesen, S. N. Coppersmith, M. A. Eriksson, *et al.*, “Gate fidelity and coherence of an electron spin in an Si/SiGe quantum dot with micromagnet,” *Proceedings of the National Academy of Sciences* **113**, 11738–11743 (2016).

²⁰R. M. Jock, N. T. Jacobson, M. Rudolph, D. R. Ward, M. S. Carroll, and D. R. Luhman, “A silicon singlet–triplet qubit driven by spin-valley coupling,” *Nature communications* **13**, 641 (2022).

²¹E. J. Connors, J. Nelson, L. F. Edge, and J. M. Nichol, “Charge-noise spectroscopy of Si/SiGe quantum dots via dynamically-decoupled exchange oscillations,” *Nature communications* **13**, 940 (2022).

²²K. Eng, T. D. Ladd, A. Smith, M. G. Borselli, A. A. Kiselev, B. H. Fong, K. S. Holabird, T. M. Hazard, B. Huang, P. W. Deelman, *et al.*, “Isotopically enhanced triple-quantum-dot qubit,” *Science advances* **1**, e1500214 (2015).

²³O. Dial, M. D. Shulman, S. P. Harvey, H. Bluhm, V. Umansky, and A. Yacoby, “Charge noise spectroscopy using coherent exchange oscillations in a singlet-triplet qubit,” *Physical review letters* **110**, 146804 (2013).

²⁴A. Anferov, S. P. Harvey, F. Wan, J. Simon, and D. I. Schuster, “Superconducting qubits above 20 GHz operating over 200 mK,” *PRX Quantum* **5**, 030347 (2024).

²⁵C. H. Yang, R. Leon, J. Hwang, A. Saraiva, T. Tanttu, W. Huang, J. Camirand Lemyre, K. W. Chan, K. Tan, F. E. Hudson, *et al.*, “Operation of a silicon quantum processor unit cell above one kelvin,” *Nature* **580**, 350–354 (2020).

²⁶J. Y. Huang, R. Y. Su, W. H. Lim, M. Feng, B. van Straaten,

- B. Severin, W. Gilbert, N. Dumoulin Stuyck, T. Tanttu, S. Serrano, *et al.*, “High-fidelity spin qubit operation and algorithmic initialization above 1 K,” *Nature* **627**, 772–777 (2024).
- ²⁷A. Shearow, G. Koolstra, S. J. Whiteley, N. Earnest, P. S. Barry, F. J. Heremans, D. D. Awschalom, E. Shirokoff, and D. I. Schuster, “Atomic layer deposition of titanium nitride for quantum circuits,” *Applied Physics Letters* **113** (2018).
- ²⁸J. Majer, J. Chow, J. Gambetta, J. Koch, B. Johnson, J. Schreier, L. Frunzio, D. Schuster, A. A. Houck, A. Wallraff, *et al.*, “Coupling superconducting qubits via a cavity bus,” *Nature* **449**, 443–447 (2007).
- ²⁹G. Koolstra, G. Yang, and D. I. Schuster, “Coupling a single electron on superfluid helium to a superconducting resonator,” *Nature communications* **10**, 5323 (2019).
- ³⁰G. Koolstra, E. Glen, N. Beysengulov, H. Byeon, K. Castoria, M. Sammon, B. Dizdar, C. Wang, D. Schuster, S. Lyon, *et al.*, “High-impedance resonators for strong coupling to an electron on helium,” *arXiv preprint arXiv:2410.19592* (2024).
- ³¹P. Harvey-Collard, G. Zheng, J. Dijkema, N. Samkharadze, A. Sammak, G. Scappucci, and L. M. Vandersypen, “On-chip microwave filters for high-impedance resonators with gate-defined quantum dots,” *Physical Review Applied* **14**, 034025 (2020).
- ³²X. Zhang, Z. Zhu, N. Ong, and J. Petta, “High-impedance superconducting resonators and on-chip filters for circuit quantum electrodynamics with semiconductor quantum dots,” *Physical Review Applied* **21**, 014019 (2024).
- ³³C. Müller, J. H. Cole, and J. Lisenfeld, “Towards understanding two-level-systems in amorphous solids: insights from quantum circuits,” *Reports on Progress in Physics* **82**, 124501 (2019).
- ³⁴B. Sarabi, A. N. Ramanayaka, A. L. Burin, F. C. Wellstood, and K. D. Osborn, “Projected dipole moments of individual two-level defects extracted using circuit quantum electrodynamics,” *Physical review letters* **116**, 167002 (2016).
- ³⁵C.-C. Hung, L. Yu, N. Foroozani, S. Fritz, D. Gerthsen, and K. D. Osborn, “Probing hundreds of individual quantum defects in polycrystalline and amorphous alumina,” *Physical Review Applied* **17**, 034025 (2022).
- ³⁶M. Hegedüs, R. Banerjee, A. Hutchison, T. Barker, S. Mahashabde, A. Danilov, S. Kubatkin, V. Antonov, and S. de Graaf, “In-situ scanning gate imaging of individual two-level material defects in live superconducting quantum circuits,” *arXiv preprint arXiv:2408.16660* (2024).
- ³⁷J. Bylander, S. Gustavsson, F. Yan, F. Yoshihara, K. Harrabi, G. Fitch, D. G. Cory, Y. Nakamura, J.-S. Tsai, and W. D. Oliver, “Noise spectroscopy through dynamical decoupling with a superconducting flux qubit,” *Nature Physics* **7**, 565–570 (2011).
- ³⁸L. Cywiński, R. M. Lutchyn, C. P. Nave, and S. Das Sarma, “How to enhance dephasing time in superconducting qubits,” *Physical Review B* **77**, 174509 (2008).
- ³⁹J. Medford, L. Cywiński, C. Barthel, C. Marcus, M. Hanson, and A. Gossard, “Scaling of dynamical decoupling for spin qubits,” *Physical review letters* **108**, 086802 (2012).
- ⁴⁰J. Burnett, A. Bengtsson, M. Scigliuzzo, D. Niepce, M. Kudra, P. Delsing, and J. Bylander, “Decoherence benchmarking of superconducting qubits. npj quantum inf. 5,” (2019).
- ⁴¹A. Vepsäläinen, R. Winik, A. H. Karamlou, J. Braumüller, A. D. Paolo, Y. Sung, B. Kannan, M. Kjaergaard, D. K. Kim, A. J. Melville, *et al.*, “Improving qubit coherence using closed-loop feedback,” *Nature Communications* **13**, 1932 (2022).
- ⁴²T. Nakajima, Y. Kojima, Y. Uehara, A. Noiri, K. Takeda, T. Kobayashi, and S. Tarucha, “Real-time feedback control of charge sensing for quantum dot qubits,” *Physical Review Applied* **15**, L031003 (2021).
- ⁴³A. A. Houck, J. Koch, M. H. Devoret, S. M. Girvin, and R. J. Schoelkopf, “Life after charge noise: recent results with transmon qubits,” *Quantum Information Processing* **8**, 105–115 (2009).
- ⁴⁴M. Metcalfe, E. Boaknin, V. Manucharyan, R. Vijay, I. Siddiqi, C. Rigetti, L. Frunzio, R. Schoelkopf, and M. Devoret, “Measuring the decoherence of a qutrit qubit with the cavity bifurcation amplifier,” *Physical Review B* **76**, 174516 (2007).
- ⁴⁵J. Lisenfeld, C. Müller, J. H. Cole, P. Bushev, A. Lukashenko, A. Shnirman, and A. V. Ustinov, “Measuring the temperature dependence of individual two-level systems by direct coherent control,” *Physical review letters* **105**, 230504 (2010).
- ⁴⁶A. J. Leggett, S. Chakravarty, A. T. Dorsey, M. P. Fisher, A. Garg, and W. Zwerger, “Dynamics of the dissipative two-state system,” *Reviews of Modern Physics* **59**, 1 (1987).
- ⁴⁷X. Jin, A. Kamal, A. Sears, T. Gudmundsen, D. Hover, J. Miloshi, R. Slattery, F. Yan, J. Yoder, T. Orlando, *et al.*, “Thermal and residual excited-state population in a 3D transmon qubit,” *Physical Review Letters* **114**, 240501 (2015).
- ⁴⁸V. Champain, V. Schmitt, B. Bertrand, H. Niebojewski, R. Maurand, X. Jehl, C. Winkelmann, S. De Franceschi, and B. Brun, “Real-time millikelvin thermometry in a semiconductor-qubit architecture,” *Physical Review Applied* **21**, 064039 (2024).
- ⁴⁹L. Petit, J. Boter, H. Eenink, G. Droulers, M. Tagliaferri, R. Li, D. Franke, K. Singh, J. Clarke, R. Schouten, *et al.*, “Spin lifetime and charge noise in hot silicon quantum dot qubits,” *Physical review letters* **121**, 076801 (2018).
- ⁵⁰M. Reagor, W. Pfaff, C. Axline, R. W. Heeres, N. Ofek, K. Sliwa, E. Holland, C. Wang, J. Blumoff, K. Chou, *et al.*, “Quantum memory with millisecond coherence in circuit qed,” *Physical Review B* **94**, 014506 (2016).
- ⁵¹M. Mehmandoust and V. Dobrovitski, “Decoherence induced by a sparse bath of two-level fluctuators: Peculiar features of $1/f$ noise in high-quality qubits,” *Physical Review Research* **6**, 033175 (2024).
- ⁵²A. V. Kuhlmann, J. Houel, A. Ludwig, L. Greuter, D. Reuter, A. D. Wieck, M. Poggio, and R. J. Warburton, “Charge noise and spin noise in a semiconductor quantum device,” *Nature Physics* **9**, 570–575 (2013).
- ⁵³X. You, A. A. Clerk, and J. Koch, “Positive-and negative-frequency noise from an ensemble of two-level fluctuators,” *Physical Review Research* **3**, 013045 (2021).
- ⁵⁴W. Zheng, K. Bian, X. Chen, Y. Shen, S. Zhang, R. Stöhr, A. Denisenko, J. Wrachtrup, S. Yang, and Y. Jiang, “Coherence enhancement of solid-state qubits by local manipulation of the electron spin bath,” *Nature Physics* **18**, 1317–1323 (2022).

Supplemental Information for Noise-resilient solid host for electron qubits above 100 mK

Xinhao Li,^{1,2} Christopher S. Wang,³ Brennan Dizdar,³ Yizhong Huang,^{4,5} Yutian Wen,⁶
Wei Guo,^{7,8} Xufeng Zhang,⁵ Xu Han,^{1,4,*} Xianjing Zhou,^{7,8,†} and Dafei Jin^{1,6,‡}

¹*Center for Nanoscale Materials, Argonne National Laboratory, Lemont, Illinois 60439, USA*

²*Department of Physics, Harvard University, Cambridge, Massachusetts 02138, USA*

³*James Franck Institute and Department of Physics, University of Chicago, Chicago, Illinois 60637, USA*

⁴*Pritzker School of Molecular Engineering, University of Chicago, Chicago, Illinois 60637, USA*

⁵*Department of Electrical and Computer Engineering, Northeastern University, Boston, Massachusetts 02115, USA*

⁶*Department of Physics and Astronomy, University of Notre Dame, Notre Dame, Indiana 46556, USA*

⁷*National High Magnetic Field Laboratory, Tallahassee, Florida 32310, USA*

⁸*Department of Mechanical Engineering, FAMU-FSU College of Engineering,
Florida State University, Tallahassee, Florida 32310, USA*

(Dated: February 19, 2025)

CONTENTS

I. Titanium nitride resonator	1
A. TiN thin film	1
B. Resonator and filter	2
II. System characterization before and after electron emission	2
III. Summary of qubit properties	3
IV. Qubit 1 (Q1) supporting data	3
A. Qubit spectroscopy	3
B. Qubit frequency drift	4
C. Thermal population	5
V. Qubit 2 (Q2) supporting data	5
A. Spectroscopic and coherence characterization	5
B. Dephasing time and noise spectroscopy	5
C. Temperature-dependent coherence	6
VI. Qubit 3 (Q3) supporting data	8
A. Spectroscopic and coherence characterization	8
B. Dephasing time and noise spectroscopy	9
References	10

I. TITANIUM NITRIDE RESONATOR

eNe qubits were coupled with titanium nitride (TiN) high-impedance superconducting resonators. In this section, we describe the details of the resonator device.

A. TiN thin film

30 nm TiN thin film was grown on intrinsic (111) Silicon via atomic layer deposition following the procedure in ref. ¹. Figure S1a plots the sheet resistance as the function of substrate temperature measured by a physical property measurement system. The kinetic inductance of the film is estimated with (ref. ¹):

$$L_k = \hbar R_{\square} / \pi \Delta_0 \quad (\text{S1})$$

Where R_{\square} is the normal sheet resistance measured just above T_c , and $\Delta_0 = 1.76 k_b T_c$ is the superconducting energy gap for TiN. With the measured $T_c = 3.8$ K and $R_{\square} = 64.42 \Omega/\square$, the estimated kinetic inductance $L_k = 23.4$ pH/ \square .

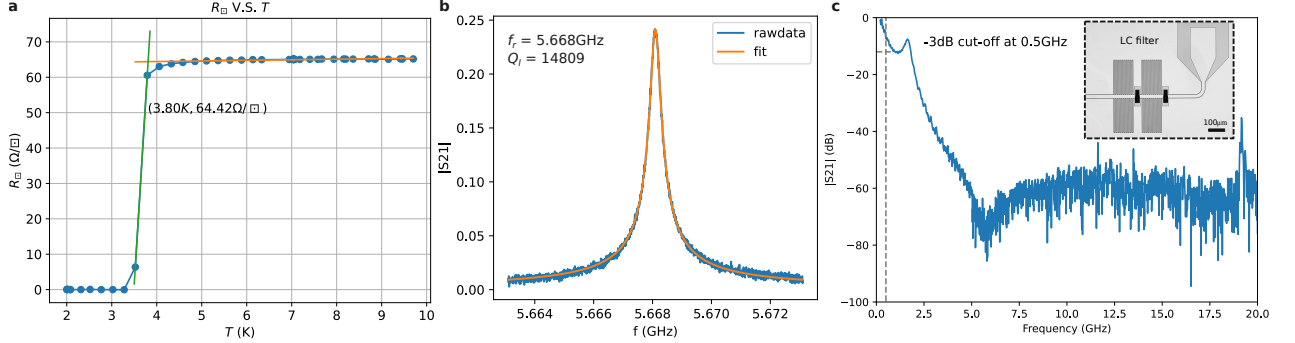


Fig. S1. Titanium nitride (TiN) thin film and resonator. **a**, Sheet resistance of 30 nm TiN film on intrinsic $\langle 111 \rangle$ Silicon substrate. **b**, Transmission spectrum of the resonator's differential mode. **c**, Transmission through the on-chip LC low pass filter. Inset: Microscope photo of the filter.

B. Resonator and filter

Figure S1b plots the measured and fitted differential mode at 5.6681 GHz, with loaded quality factor $Q_l = 14809$, or equivalent resonator linewidth $\kappa/2\pi = 0.38$ MHz. We estimated the resonator's $\lambda/2$ differential mode impedance with the equivalent lumped element model of a split superconducting resonator (ref. ^{2,3}):

$$\omega_{diff} = \frac{1}{\sqrt{L_{diff} C_{diff}}} \quad (\text{S2})$$

$$L_{diff} = \frac{2L_l l}{\pi^2} \quad (\text{S3})$$

$$Z_{diff} = \sqrt{\frac{L_{diff}}{C_{diff}}} \quad (\text{S4})$$

Where $l = 1061 \mu\text{m}$ is the length of the inductance part of the resonator. For a split resonator, self and mutual inductance contribute to the total inductance as $L_l = L_{self} + |L_{mutal}|$. Here, we estimated $L_l \simeq L_k/w = 7.8 \times 10^{-5}$ H/m, where resonator width $w = 0.3 \mu\text{m}$, neglecting the mutual inductance due to the large distance between the two resonator pins and the minor geometry contribution to the self-inductance. Following the model, the equivalent $L_{diff} = 1.68 \times 10^{-8}$ H and $C_{diff} = 4.69 \times 10^{-14}$ F. The calculated equivalent differential mode impedance is $Z_{diff} = 598.5 \Omega$. Given the qubit-resonator coupling strength $g \propto \omega_r \sqrt{Z_r}$ (ref. ³), the TiN resonator should improve the coupling strength by about 2.85 times compared with the previous niobium resonator with equivalent lumped element impedance of $\sim 57.3 \Omega$ and differential mode at 6.42 GHz (ref. ⁴).

To maintain the resonator's quality factor, on-chip LC filters are attached to all DC electrodes near the electron trap and to the center bias on the resonator. Figure S1c plots the measured transmission through the LC filter showing broadband ~ 60 dB isolation above 4 GHz with a 3 dB cut-off frequency at 0.5 GHz.

II. SYSTEM CHARACTERIZATION BEFORE AND AFTER ELECTRON EMISSION

We run control experiments to show the effects of neon on electron trapping. Figure S2 plots the representative resonator spectroscopies while sweeping the resonator voltage for four situations, i.e., with or without neon deposition

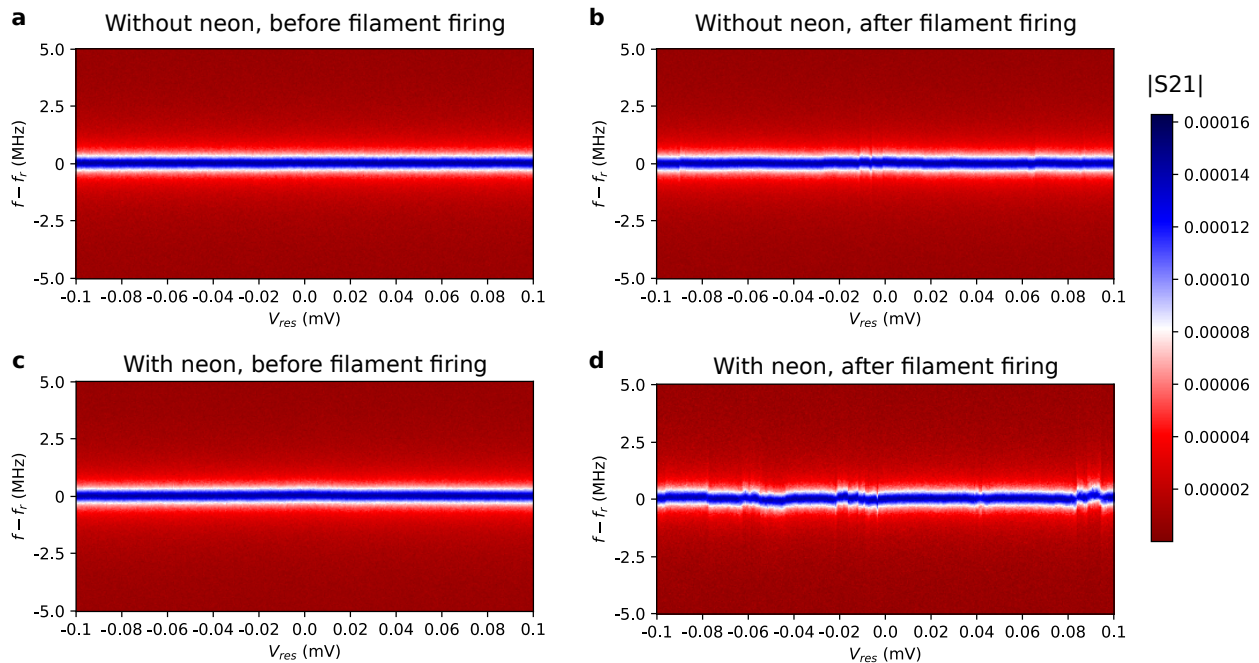


Fig. S2. Resonator response to electron emission. Representative instance of resonator spectroscopy versus V_{res} without (a, b) and with (c, d) neon deposition, and before (a, c) and after (b, d) emitting electrons onto the device. Qualitatively, the number and strength of anti-crossing features increase under the condition after firing filament on the neon-covered resonator.

and before or after emitting electrons from the tungsten filament. Before firing the filament or without neon, we rarely observe strong couplings. We fire the filament following the same procedure as in the Methods of the main text. We observed a significant increase in both the number and strength of anti-crossing features over the same voltage range only when the resonator is covered with a thin layer of neon. We interpret these features as originating from both trapped eNe qubits and floating electrons with high mobility near the resonator electrodes. These results indicate that the neon layer enables the stable trapping of electrons strongly coupled with the resonator. For a typical experiment, we then zoom in to conduct refined scanning near the anti-crossings to characterize the qubit spectroscopy, followed by time-domain coherence measurements. Only when both the neon film is present on the sample surface and electrons are emitted, are we able to characterize eNe qubits with vacuum Rabi splitting, two-tone qubit spectroscopy, and time domain measurements.

III. SUMMARY OF QUBIT PROPERTIES

This section summarizes the properties of the three eNe qubits tested in this work.

	f_{ss} (GHz)	T_1 (μ s)	T_2^* (μ s)	T_2^{echo} (μ s)	N to approach $2T_1$	$g/2\pi$ (MHz)
Qubit 1	5.065	11.6	8.2	21.6	2	6.43
Qubit 2	5.699	25.1	7.2	25.2	64	6.17
Qubit 3	4.456	74.3	3.5	4.0	128	16

Tab. SI. Summary of the three eNe qubits properties at charge sweet-spot.

IV. QUBIT 1 (Q1) SUPPORTING DATA

A. Qubit spectroscopy

Figure S3a plots the data and fit of the transmission spectrum when the qubit is in resonance with the resonator. Fitting to the input-output theory model gives the qubit-resonator coupling strength $g/2\pi = 6.43$ MHz and qubit

linewidth $\gamma/2\pi = 3.18$ MHz.

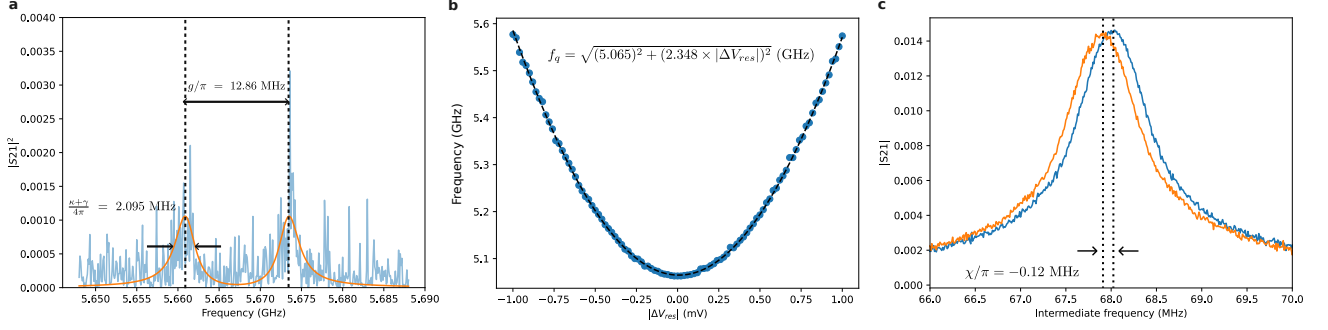


Fig. S3. Qubit 1 spectroscopy data. **a**, Measurement and fitting of transmission spectrum when Q1 is on resonance with the resonator. **b**, Fitting of the qubit spectrum to the model in the main text. **c**, Resonator dispersive shift measurement when Q1 is biased at its charge sweet-spot.

Figure S3b plots the qubit spectrum with the transition frequency extracted from Fig. 2b in the main text. We fit the qubit spectrum to $f_q = \sqrt{(2.348 \times 10^9 \Delta V_{res})^2 + (5.065 \times 10^9)^2}$, with f_q in the unit of Hz and ΔV_{res} in the unit of mV. The equivalent ΔV_{res} and qubit sensitivity to voltage fluctuation in the main text is calculated based on this fitting result, given the measured qubit frequency at different basis points.

Figure S3c plots the transmission spectrum through the resonator when the qubit is prepared at the ground state (blue curve) or excited state (orange curve) biased at its charge sweet-spot. The measurement indicates a dispersive shift $\chi/\pi = -0.12$ MHz.

B. Qubit frequency drift

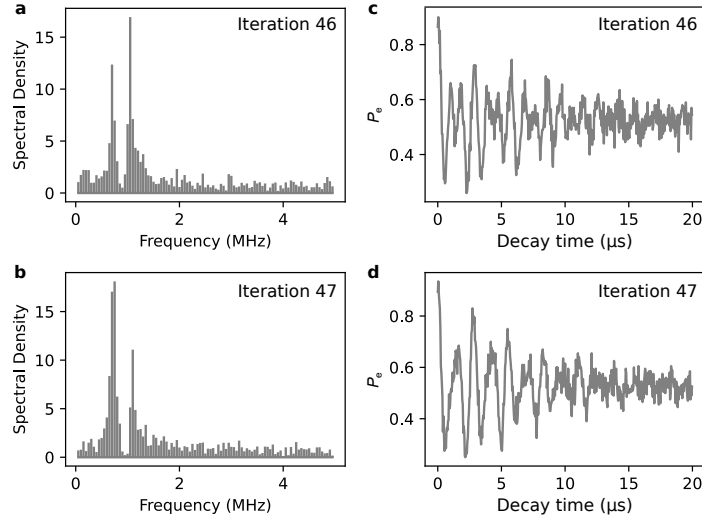


Fig. S4. Qubit 1 frequency drift. **a** and **b**, Frequency components of Ramsey measurements in iterations 46 and 47. **c** and **d**, Raw data of Ramsey measurements in iterations 46 and 47.

Figure S4 plots the measured Ramsey fringes in iterations 46 and 47, whose frequency components show double peaks. These results reveal a slow drift of the qubit frequency during the one-minute measurement.

C. Thermal population

Figure S5 plots the measured thermal population of Q1 versus the mixing chamber (MXC) temperature. The data match well with calculated results based on a Maxwell-Boltzmann model⁵, considering only the first two qubit states, $P_e = 1/(1 + 1/\exp(-\hbar\omega_q/k_bT))$, where ω_q is the qubit frequency at the sweet-spot. We also used the MXC temperature as the T to calculate the solid curve in Fig. S5.

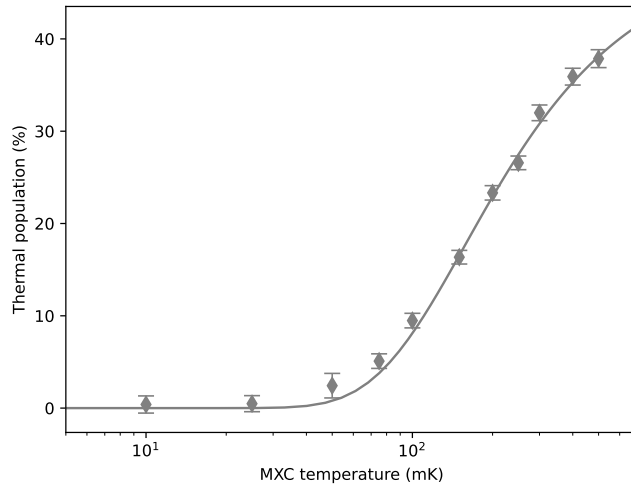


Fig. S5. Thermal population of Q1 versus MXC temperature. Thermal population of Q1 (gray diamonds, data) along with the predicted population (gray solid curve) from a Maxwell-Boltzmann distribution model with no fit parameters.

V. QUBIT 2 (Q2) SUPPORTING DATA

Q2 was trapped on a different resonator fabricated within the same batch as the one used to trap Q1. The resonator has a differential mode at 5.870 GHz with a resonator linewidth of $\kappa/2\pi = 0.53$ MHz. We performed noise characterization with dynamical decoupling methods when it was biased on and off the charge sweet-spot. We also characterized its temperature-dependent coherence performance on the charge sweet-spot. The details of the data are shown in this section.

A. Spectroscopic and coherence characterization

Figure S6a plots the vacuum Rabi splitting (top panel) and the two-tone qubit spectrum versus the relative bias voltage on the resonator ΔV_{res} . Same as Q1, Q2 is insensitive to voltage bias applied on the resonator and trap guard, as shown in Fig. 1 of the main text. By fitting the on-resonance transmission spectrum, as shown in Fig. S6b, we extract the qubit-resonator coupling strength of $g/2\pi = 6.17$ MHz and qubit linewidth of $\gamma/2\pi = 5.84$ MHz. Figure S6c plots the extracted qubit spectrum of $f_q = \sqrt{(5.699 \times 10^9)^2 + (1.516 \times 10^9 \Delta V_{res})^2}$, with f_q in unit of Hz and ΔV_{res} in unit of mV. Figure S6d-e show the measured $T_1 = 25.1 \mu s$, $T_2^* = 7.2 \mu s$, and $T_2^{echo} = 25.2 \mu s$ at the charge sweet-spot. Figure S6f shows that with refocusing pulses, the T_2^{CPMG} increases to approach $2T_1$ when biased at the sweet-spot.

B. Dephasing time and noise spectroscopy

Figure S7a plots the calculated T_2^{CPMG} as a function of refocusing pulse number $N = 0, 1, 2, 4, 8, 16, 32, 64$ for Q2 biased at different ΔV_{res} and sensitivity to voltage fluctuation $|\partial f_q/\partial \Delta V_{res}|$. With an increase in the refocusing pulse number, T_2^{CPMG} all approach $2T_1$. When the qubit is biased to be more sensitive to charge noise, more refocusing

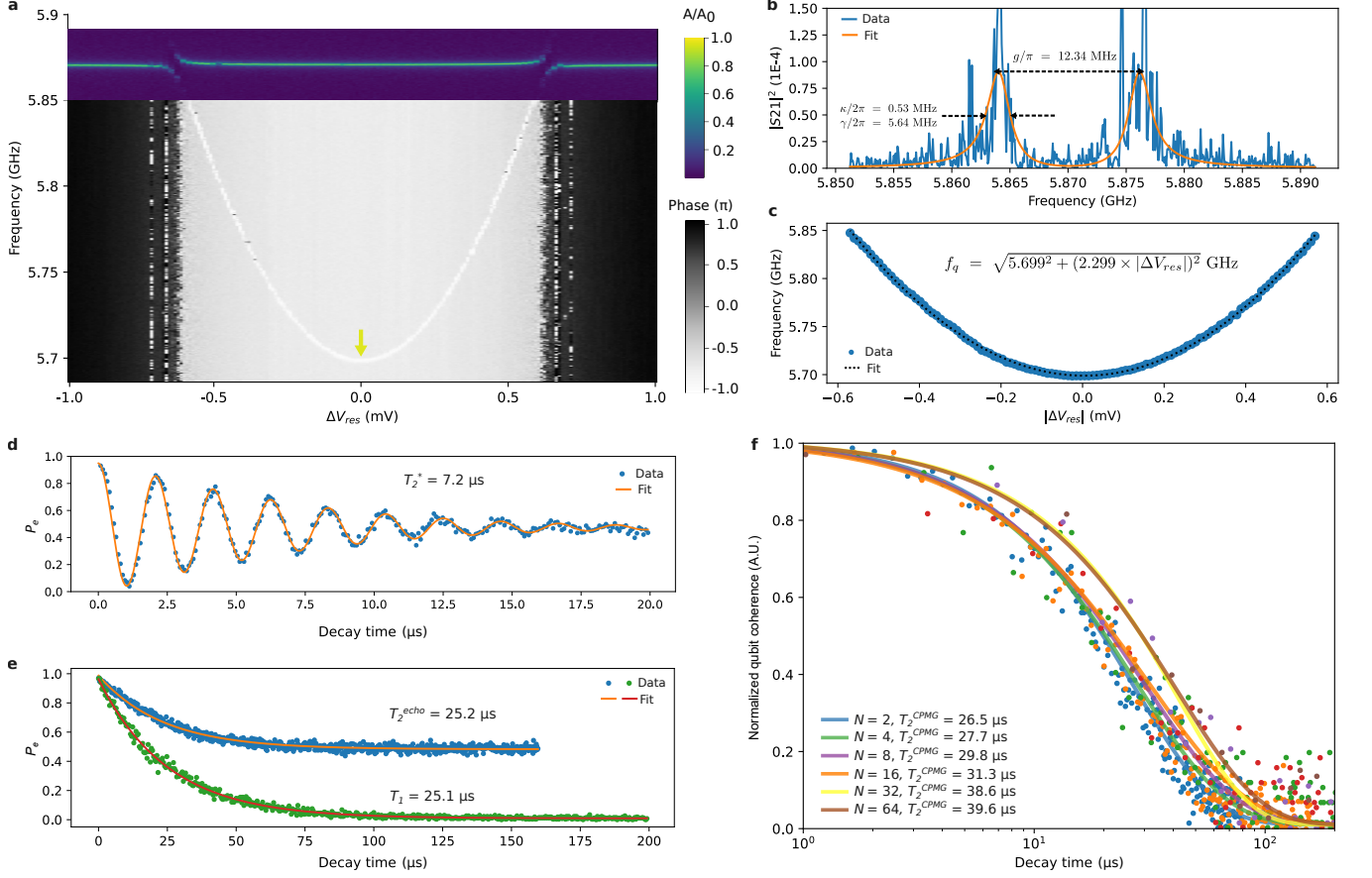


Fig. S6. Qubit 2 spectroscopy and coherence at charge sweet-spot **a**, Vacuum Rabi splitting and qubit spectrum as the function of ΔV_{res} . **b**, Measurement and fitting of transmission spectrum when Q2 is in resonance with the resonator. **c**, Fitting of the qubit spectrum to the model in the main text. **d**, Ramsey fringes at the charge sweet-spot. **e**, Energy relaxation and Hahn echo measurement at the charge sweet-spot. **f**, Coherence time extended by dynamical decoupling with CPMG pulses sequence at the charge sweet-spot.

pulses are needed to mitigate high-frequency noise to push T_2^{CPMG} towards the relaxation limit. Figure S7b plots the fitted pure dephasing time T_ϕ as the function of N and $|\partial f_q / \partial \Delta V_{res}|$. Unlike Q1 in the main text, Q2 suffers from more significant high-frequency noise when biased at its charge sweet-spot, requiring more refocusing pulses to increase T_ϕ . Besides, the power-law fittings for data acquired on and off the charge sweet-spot are distinct. On the sweet-spot, $T_\phi \propto N^{0.22}$. In contrast, when away from the sweet-spot $T_\phi \propto N^{0.47}$. This observation indicates that the charge noise dominates the qubit decoherence when it is biased away from the charge sweet spot. As shown in Fig. S7c, we calculate the total noise measured by the dynamical decoupling method between 10 kHz and 1 MHz. The power-law fittings of the data on and off the charge sweet-spot further confirm the different spectra distribution of $S \propto 1/f^{0.26}$ and $S \propto 1/f^{0.97}$. Extracting the noise source contributing to the dephasing when biased at the sweet-spot, we calculate the resonator electrode's equivalent charge (voltage) noise considering the qubit's sensitivity to voltage fluctuation. As shown in Fig. S7d, the calculated charge noise also falls in the range of $10^{-5} \mu V^2/Hz$, similar to the value of Q1 in the main text.

C. Temperature-dependent coherence

Figure S8a plots the T_1 versus mixing chamber (MXC) temperature when Q2 is biased at its charge sweet-spot. The blue dash curve shows the thermal decay model^{6,7}, with measured low-temperature T_1 at 10 mK as $T_1(T=0)$ and projection to the high-temperature values. At 300 mK, Q2 maintained a $T_1 = 9.31 \mu s$, about 40% of the low-

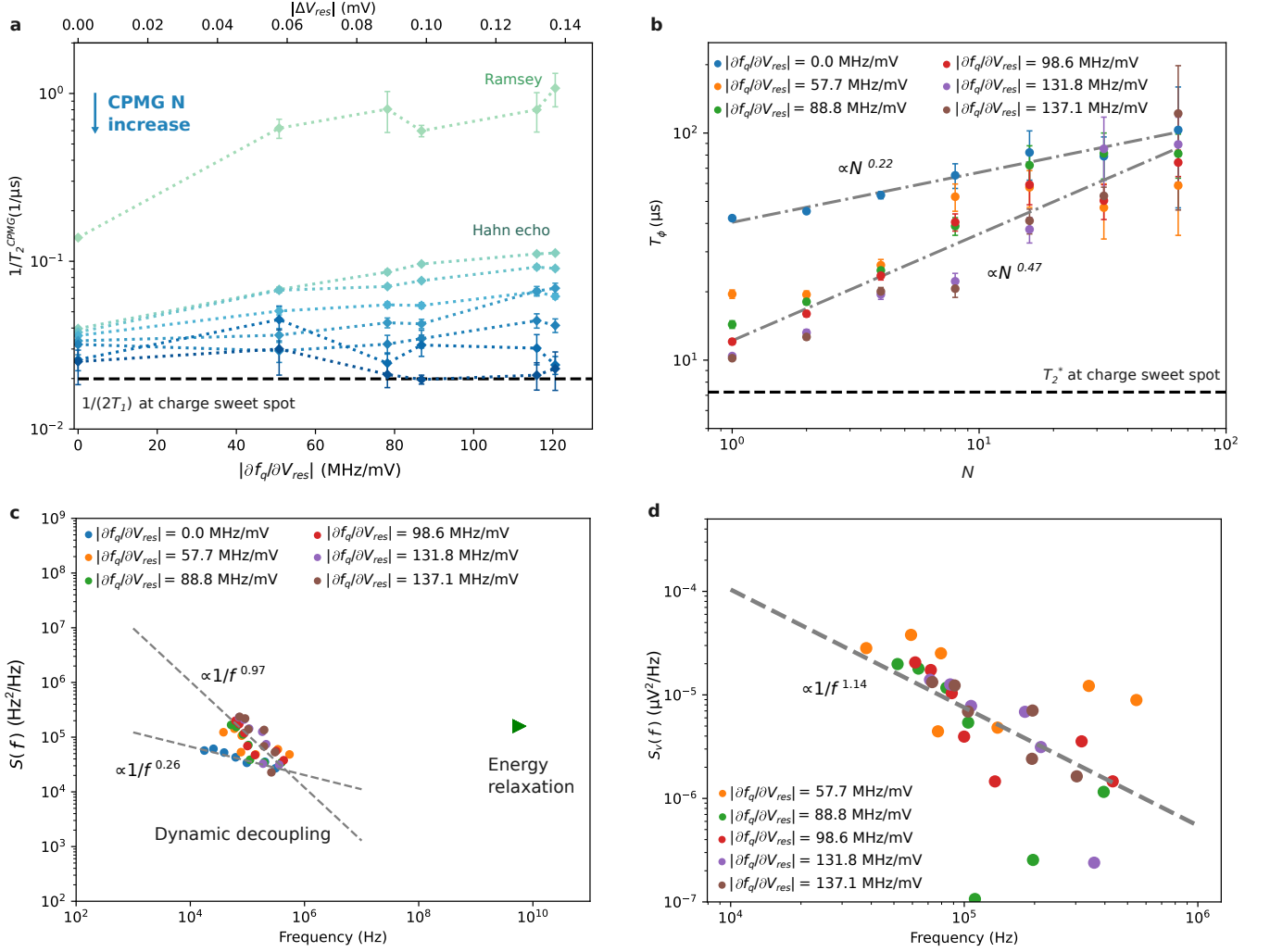


Fig. S7. Qubit 2 noise characterization with dynamical decoupling methods. **a**, Calculated $1/T_2^{CPMG}$ as the function of refocusing pulse number N and qubit's sensitivity to voltage fluctuation $|\partial f_q/\partial V_{res}|$. **b**, Fitted dephasing time T_ϕ as the function of N and $|\partial f_q/\partial V_{res}|$. **c**, Calculated total noise spectral density via dynamical decoupling methods and transverse noise due to energy relaxation. **d**, Calculated equivalent charge (voltage) noise on the resonator electrode.

temperature value. Meanwhile, the good match between the model and measured data, similar to Q1 in the main text, further confirms that thermal-induced decay dominates the degradation of T_1 at higher temperatures. Figure S8b plots the temperature-dependent T_2^* and T_2^{echo} of Q2 biased at its sweet-spot. The power-law fittings give $T_2^* \propto 1/T^{1.23}$ and $T_2^{echo} \propto 1/T^{1.68}$. The difference in the fitted exponent indicates a faster increase in high-frequency noise components with higher temperatures than low-frequency components. Figure S8c plots the extracted pure dephasing time and the calculated resonator induced dephasing based on the same model in the main text^{8,9}. The dispersive shift of the resonator when Q2 is biased at its sweet-spot is estimated by $\chi \simeq g^2/\Delta$, where g is the qubit-resonator coupling strength, and Δ is the qubit-resonator detune¹⁰. The model matches well to the high-temperature values of T_ϕ .

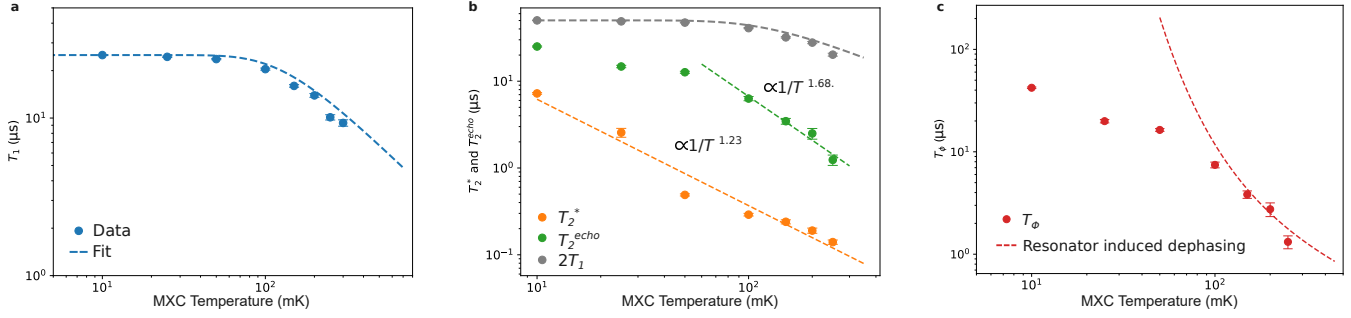


Fig. S8. Temperature-dependent coherence of Qubit 2. **a**, T_1 versus mixing chamber (MXC) temperature, with projection based on the thermal decay model $T_1(T) = T_1(T=0) \cdot \tanh(\hbar\omega_q/2k_B T)$. We use the measured T_1 at 10 mK as $T_1(T=0)$. **b**, T_2^* and T_2^{echo} versus MXC temperature, with power-law fitting. Gray dots and the dashed curve show the value of $2T_1$. **c**, Pure dephase time T_ϕ versus MXC temperature, with a parameter-free calculation based on resonator induced dephasing model.

VI. QUBIT 3 (Q3) SUPPORTING DATA

Q3 was trapped on the same resonator used to trap Q1 in the main text. During its short trapping lifetime, we managed to characterize its coherence properties at the charge sweet-spot. This section will focus on reporting the relevant data.

A. Spectroscopic and coherence characterization

Figure S9a plots the vacuum Rabi splitting versus the relative bias voltage on the resonator ΔV_{res} . Figure S9b shows the zoom-in plot of right splitting when adjusting the resonator guard electrode. The fit of avoided crossing gives a coupling strength of $g/2\pi \simeq 16$ MHz. We could not resolve the two transmission peaks when the qubit is in resonance with the resonator, indicating a relatively large on-resonance qubit linewidth. Figure S9c plots the theoretical calculation of the transmission spectrum with a fitted g and a qubit linewidth of $\gamma/2\pi = 15$ MHz, which qualitatively matches the experimental measurements. Figure S9d plots the two-tone measured qubit spectrum with a charge sweet-spot at 4.456 GHz. In Figure S9e-g, we show the measured $T_1 = 74.3 \mu\text{s}$, $T_2^* = 3.46 \mu\text{s}$, and $T_2^{echo} = 3.96 \mu\text{s}$ at the charge sweet-spot. With the large qubit-resonator detuning, the energy relaxation is dominated by non-radiative decay at the sweet-spot.

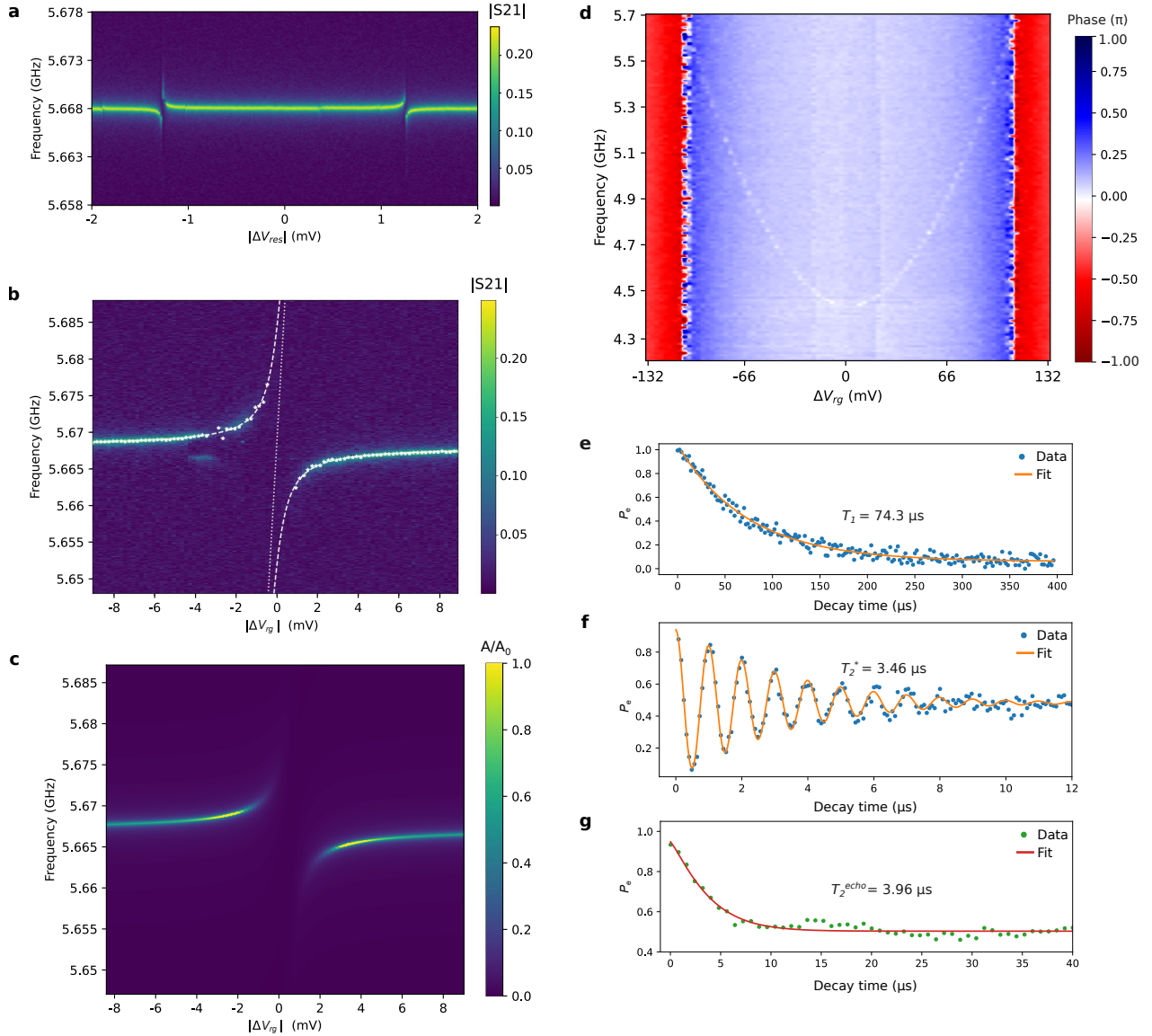


Fig. S9. Qubit 3 spectroscopy and coherence at sweet-spot. **a**, Vacuum Rabi splitting. **b**, Fitting of qubit-resonator coupling strength g . White dots and dashed curves show extracted transmission peaks and fit to the two branches of the splitting. The white dot-dashed line shows the linear fitting of the qubit spectrum near the resonator frequency. **c**, Calculation of resonator transmission spectrum with parameters acquired from fitting in **b** and qubit linewidth $\gamma/2\pi = 15$ MHz. **d**, Two-tone measured qubit spectrum. **e**, Energy relaxation, **f**, Ramsey fringes, and **g**, Hahn echo measurement at the charge sweet-spot.

B. Dephasing time and noise spectroscopy

We managed to improve the coherence time of Q3 at its sweet-spot with the dynamical decoupling method. As shown in Fig. S10a-b, T_2^{CPMG} increased to be above $100 \mu\text{s}$ when 64 refocusing pulses are applied. Similar to Q2, Q3 experienced significant high-frequency noise components when biased at its sweet-spot. The inconsistency in total noise distribution on the charge sweet-spot among the three qubits indicates the complexity of noise sources for the eNe charge qubit. Figure S10c plots the fitted T_ϕ as the function of N , with a power-law fitting of $T_\phi \propto N^{0.77}$. Figure S10d shows the extracted total noise spectral density near the 0.1 MHz range, with similar absolute values as Q1 and Q2.

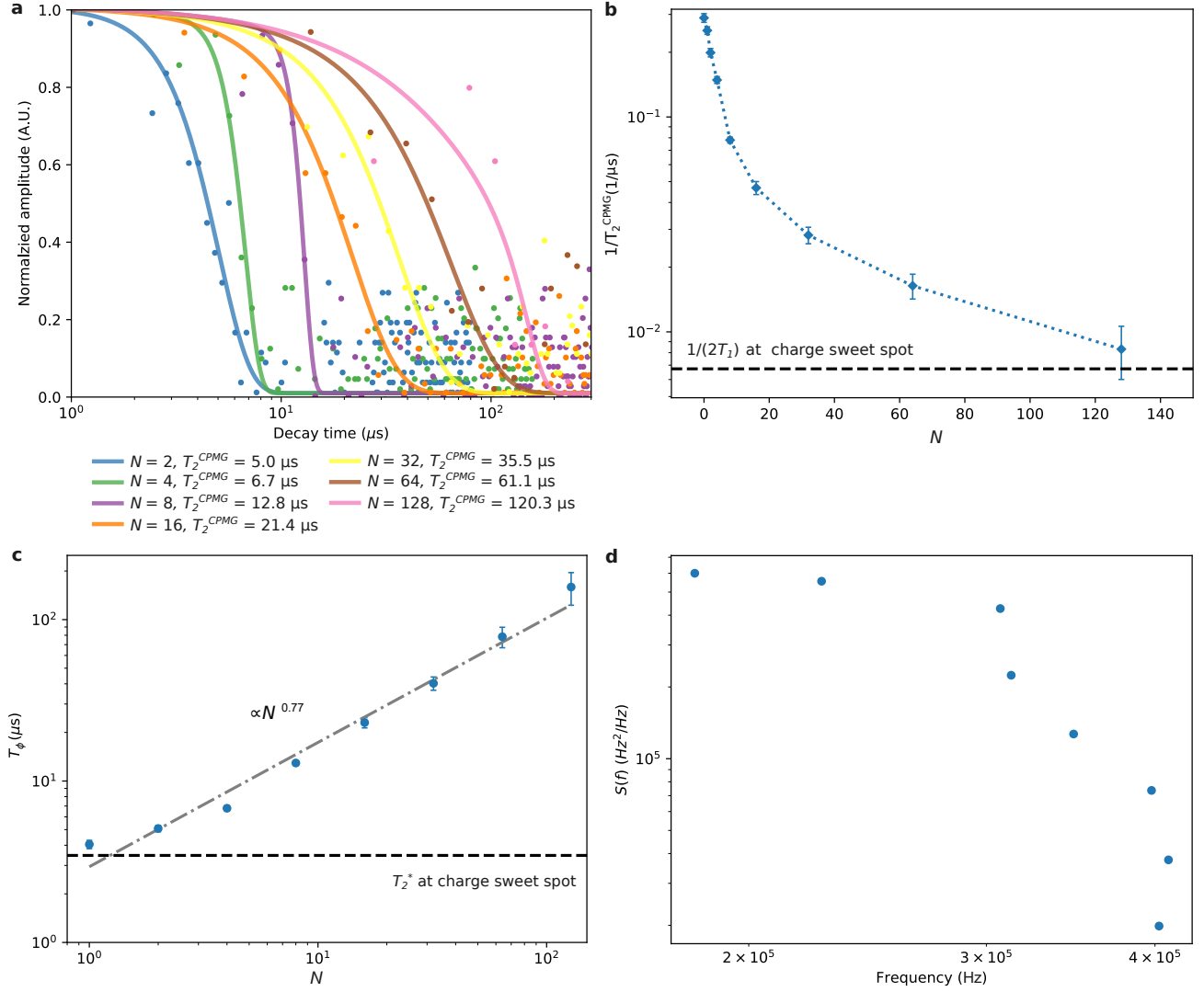


Fig. S10. Dynamical decoupling and noise characterization of Qubit 3 at the sweet-spot. **a**, Extension of coherence time via dynamical decoupling with CPMG pulse sequence. **b**, Calculated $1/T_2^{\text{CPMG}}$ as the function of refocusing pulse number N . **c**, Fitted pure dephasing time T_ϕ as the function of N . **d**, Calculated total noise spectral density near 0.1 MHz characterized via dynamical decoupling methods.

* Email: xu.han@anl.gov

† Email: xianjing.zhou@cea.fr

‡ Email: dfjin@nd.edu

¹ A. Shearrow, G. Koolstra, S. J. Whiteley, N. Earnest, P. S. Barry, F. J. Heremans, D. D. Awschalom, E. Shirokoff, and D. I. Schuster, *Applied Physics Letters* **113** (2018).

² G. Koolstra, G. Yang, and D. I. Schuster, *Nature communications* **10**, 5323 (2019).

³ G. Koolstra, E. Glen, N. Beysengulov, H. Byeon, K. Castoria, M. Sammon, B. Dizdar, C. Wang, D. Schuster, S. Lyon, *et al.*, arXiv preprint arXiv:2410.19592 (2024).

⁴ G. Koolstra, *Trapping a single electron on superfluid helium using a superconducting resonator*, Ph.D. thesis, The University of Chicago (2019).

⁵ X. Jin, A. Kamal, A. Sears, T. Gudmundsen, D. Hover, J. Miloshi, R. Slattery, F. Yan, J. Yoder, T. Orlando, *et al.*, *Physical Review Letters* **114**, 240501 (2015).

⁶ J. Lisenfeld, C. Müller, J. H. Cole, P. Bushev, A. Lukashenko, A. Shnirman, and A. V. Ustinov, *Physical review letters* **105**, 230504 (2010).

- ⁷ A. J. Leggett, S. Chakravarty, A. T. Dorsey, M. P. Fisher, A. Garg, and W. Zwerger, *Reviews of Modern Physics* **59**, 1 (1987).
- ⁸ A. Anferov, S. P. Harvey, F. Wan, J. Simon, and D. I. Schuster, *PRX Quantum* **5**, 030347 (2024).
- ⁹ M. Reagor, W. Pfaff, C. Axline, R. W. Heeres, N. Ofek, K. Sliwa, E. Holland, C. Wang, J. Blumoff, K. Chou, *et al.*, *Physical Review B* **94**, 014506 (2016).
- ¹⁰ D. I. Schuster, *Circuit quantum electrodynamics* (Yale University, 2007).